Journal of Medicinal Chemistry Article

J. Med. Chem. **2010,** *53,* 6301–6315 **6301**
DOI: 10.1021/jm100337z

Synthesis, in Vitro Activity, and Three-Dimensional Quantitative Structure−Activity Relationship of Novel Hydrazine Inhibitors of Human Vascular Adhesion Protein-1

Elisa M. Nurminen,[†] Marjo Pihlavisto,[‡] László Lázár,[§] Zsolt Szakonyi,[§] Ulla Pentikäinen,[†] Ferenc Fülöp,[§] and Olli T. Pentikäinen*,[†]

[†]*Department of Biological and Environmental Science & Nanoscience Center, P.O. Box 35, FI-40014 University of Jyväskylä, Finland,* [‡]*BioTie Therapies Corporation, Tykistökatu 6, FI-20520 Turku, Finland, and* [§]*Institute of Pharmaceutical Chemistry, University of Szeged, H-6720 Eotvos 6, Szeged, Hungary*

Received February 17, 2010

Vascular adhesion protein-1 (VAP-1) belongs to the semicarbazide-sensitive amine oxidases (SSAOs) that convert amines into aldehydes. SSAOs are distinct from the mammalian monoamine oxidases (MAOs), but their substrate specificities are partly overlapping. VAP-1 has been proposed as a target for anti-inflammatory drug therapy because of its role in leukocyte adhesion to endothelium. Here, we describe the synthesis and in vitro activities of novel series of VAP-1 selective inhibitors. In addition, the molecular dynamics simulations performed for VAP-1 reveal that the movements of Met211, Ser496, and especially Leu469 can enlarge the ligand-binding pocket, allowing larger ligands than those seen in the crystal structures to bind. Combining the data from molecular dynamics simulations, docking, and in vitro measurements, the three-dimensional quantitative structure−activity relationship (3D QSAR) models for VAP-1 (q^2_{LOO}: 0.636; r^2: 0.828) and MAOs (q^2_{LOO}: 0.749, r^2: 0.840) were built and employed in the development of selective VAP-1 inhibitors.

Introduction

Amine oxidases (AOs) are a group of enzymes that catalyze amine metabolism; they convert amine compounds into corresponding aldehydes with concomitant hydrogen peroxide and ammonia production. All reaction products are known to be cytotoxic at high concentrations and may play an important role in the pathogenesis of many types of vasculopathies.[1,2] AOs can be divided into two families based on their cofactors, namely, (1) posttranslationally modified amino acids [either topaquinone (TPQ[a])[3] or lysine tyrosylquinone[4] or (2) flavin. Semicarbazide-sensitive amine oxidases (SSAOs) such as vascular adhesion protein-1 (VAP-1) (EC 1.4.3.21) and diamine oxidase (EC 1.4.3.22) use TPQ as a cofactor, whereas lysyl oxidase (EC 1.4.3.13) uses lysine tyrosylquinone. Flavin-containing AOs are, for example, monoamine oxidases (MAO) A and B (EC 1.4.3.4), and polyamine oxidases (EC 1.5.3.11.). The natural substrate for VAP-1 is not known, but primary amines are known to be accepted as substrates (e.g., benzylamine and methylamine).[5] MAOs' natural substrates include, for example, neurotransmitters such as dopamine, epinephrine, and norepinephrine.[6] Both VAP-1 and MAOs can degrade serotonin and tyramine.[7]

VAP-1 has adhesive properties, in addition to its catalytic function. It is a type II transmembrane glycoprotein with a large glycosylated extracellular domain and a short N-terminal intracellular domain of four amino acids, which have a role in the adhesion of lymphocytes to endothelial cells and lymphocyte recirculation in an L-selectin-independent manner.[8,9] The crystal structures determined for human VAP-1[10,11] show that its structure is homodimeric. The active site is buried deep within the protein, including the TPQ cofactor, three conserved histidines which are coordinated to the Cu^{2+} required for TPQ biogenesis, and the catalytic base (Asp386).[10,11] The accessibility of the active site is restricted by Leu469, which blocks the entrance to the ligand binding site.[11]

Changes in the expression levels or enzymatic activity of VAP-1 are related to numerous inflammation-associated diseases such as arthritis,[12,13] type 1 and type 2 diabetes,[14−16] obesity,[17] and congestive heart failure.[18] In addition to the harmful effects of changes in expression levels of VAP-1, some reaction products, such as methylglyoxal, which is able to form advanced-glycation end-products, can be cytotoxic.[19] The number of VAP-1-related diseases and the populations they affect make them an interesting target for drug discovery. Several small molecule VAP-1 inhibitors have already been identified, such as phenylallylhydrazines,[20] thiocarbamoyl derivatives,[21] carboxamides,[22] and sulfonamides (Figure 1).[23] In addition to small molecule inhibitors, VAP-1 function can be altered by using (1) peptides with NH_3^+ functionality (lysine side chain),[24−26] (2) function blocking antibodies (that inhibit leukocyte trafficking),[27] and (3) small interfering RNAs (that inhibit both adhesion and enzymatic functions).[28] The major challenge in the design of VAP-1 inhibitors is to gain enzyme subtype selectivity against other amine oxidases.

*To whom correspondence should be addressed. Address: Department of Biological and Environmental Science & Nanoscience Center, Computational Bioscience Laboratory, P.O. Box 35, FI-40014 University of Jyväskylä, Finland. Phone: +358-14-260-4186. Fax: +358-14-260-2221. E-mail: olli.t.pentikainen@jyu.fi.

[a] Abbreviations: 3D QSAR, three dimensional quantitative structure−activity relationship; CoMSIA, comparative molecular similarity indices analysis; LOO, leave one out; MAO, monoamine oxidase; MD, molecular dynamics; PLS, partial least square; SEE, standard error of estimate; SSAO, semicarbazide-sensitive amine oxidase; TPQ, topaquinone; VAP-1, vascular adhesion protein-1.

Published on Web 08/06/2010

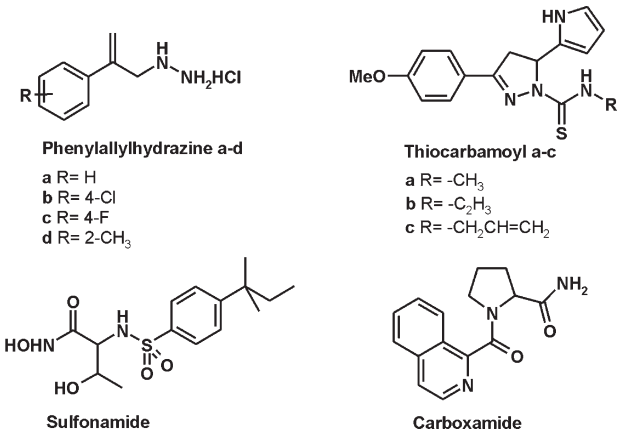

Figure 1. Structures of some known small molecule VAP-1 inhibitors. Phenylallylhydrazines a−d, thiocarbamoyl derivatives a−c, sulfonamide, and carboxamide.

Only a few molecules such as phenylallylhydrazines[20] have so far been reported to exhibit VAP-1 selectivity over MAOs. Available crystal structures for VAP-1 with bound inhibitor,[10] and for other amine oxidases such as MAO A[29,30] and MAO B,[31−34] however, enable the rational structure-based inhibitor design. The crystal structures of VAP-1[10] and MAO B[34] with bound hydrazine inhibitors reveal that the reaction mechanisms for these two enzymes are different: in MAO B the hydrazine moiety of the ligand is removed in the course of the reaction, whereas in VAP-1 it remains in the covalently bound product.

Here, we show the ability of synthesized novel 46 hydrazine molecules to inhibit VAP-1 and total MAO activities (both MAO A and B). Among these compounds, there are several molecules that are highly selective for VAP-1 over total MAO. In addition, we have investigated the flexibility of the ligand-binding pocket of VAP-1 using molecular dynamics (MD) simulations. The results reveal that the flexibility of the VAP-1 ligand-binding pocket enables the binding of much larger ligands than have thus far been shown. On the basis of the biological data and information obtained from MD simulation, we have built three-dimensional quantitative structure−activity relationship (3D QSAR) models for VAP-1 and total MAO. Both 3D QSAR models are based on the same ligand superposition, allowing a rapid prediction not only of inhibitor potency but also of inhibitor selectivity between VAP-1 and total MAO. This is advantageous for VAP-1 ligand discovery, since only one docking simulation is needed. To further validate the quality of these 3D QSAR models, novel VAP-1 inhibitors were developed by employing the models.

Results and Discussion

Synthesis. The N^1,N^1-disubstituted hydrazines **3a**−**s** (Table 1) were prepared starting from the corresponding secondary amines **1a**−**s** by a conventional two-step procedure,[35,36] including *N*-nitrosation and subsequent $LiAlH_4$ reductions of the *N*-nitroso intermediates **2a**−**s** (Scheme 1).

Unsubstituted hydrazino alcohols **5** and **6** were synthesized by ring-opening reactions of the corresponding styrene oxides **4a**−**c** with hydrazine hydrate, resulting in a mixture of the regioisomeric products **5** and **6** in a ratio of ca. 2:1 (Scheme 2).[37] For the unsubstituted compounds **5a** and **6a**, both isomers could be isolated by fractional crystallization of their hydrogen maleate salt. For the methoxy-substituted derivatives, this separation procedure could only result in the main products (**5b**,**c**), and all of our efforts to isolate the minor isomers (**6b**,**c**) failed (Scheme 2).

The synthesis of 1,2-hydrazino alcohols **9a**−**j** and **10a**−**d** (Table 1) was also accomplished by sequential nitrosation and reduction reactions starting from the corresponding amino alcohol **7**. C-Unsubstituted 1,2-amino alcohols (**7**: $R^3 = R^4 = H$) were obtained by the ring-opening reactions of the corresponding styrene oxides with amines.[38,39] Ephedrine-homologue amino alcohols (**7**: R^3 = Et, Pr, R^4 = H; or $R^3 = R^4$ = Me) were also prepared by using the methods described in the literature.[40−42] The *N*-nitroso intermediates **8** were also converted to their *O*-methyl derivatives (**11**),[43,44] the $LiAlH_4$ reduction of which resulted in hydrazino ethers **12a**−**j** (Scheme 3).

In Vitro Activity. In vitro potency was determined for the synthesized inhibitors **3a**−**3s**, **9a**−**9j**, **12a**−**12j**, and **10a**−**10d** (Table 1). The results indicate that most of the compounds are specific inhibitors of human VAP-1 activity. The IC_{50} for VAP-1 inhibition varies from 20 nM to 2.24 μM, which is 110-fold variation in inhibition (Table 1). The major differences were in the selectivity of inhibitors against the total MAO potency, with selectivity ranging from 6- to 200-fold (Table 1).

Flexibility of the Ligand-Binding Pocket. All synthesized compounds are larger (Table 1) than the 2-hydrazinopyridine seen in the only crystal structure of VAP-1 with a bound inhibitor.[10] The biological data (Table 1) also show that notably larger compounds also bind strongly to VAP-1, for example, compounds **3b**, **3f**, **3o**, and **5a**−**c** (Table 1). For future improvement of VAP-1 inhibitors, it is crucial to understand how the conformation of the ligand-binding pocket changes when larger inhibitor molecules bind. The flexibility of the ligand-binding pocket was hence examined using MD simulations with a bound ligand. In particular, we wanted to investigate the flexibility of Leu469, as Leu469 seems to act as a gate residue into the substrate binding site.[11] From the synthesized molecules, compounds **5a**−**c** (Table 1) have a hydrogen atom and a hydroxyl group at positions R1 and R2, respectively, binds more strongly to VAP-1 than those having a methyl group or larger at position R1 (**9a**−**9j**, Table 1) or methyl and methoxy groups at positions R1 and R2, respectively (**12a**−**j**, Table 1). As the size of the aryl group is not critical for binding to VAP-1 (Table 1, compounds **5a**−**c**), the molecule **5a** was chosen for MD simulations, as it has the simplest structure and shows strong binding and good VAP-1 selectivity over total MAO (Table 1).

In the crystal structure of VAP-1 with the bound inhibitor 2-hydrazinopyridine, Leu469 is in a conformation where its side chain blocks the ligand-binding cavity (Figure 2A,B). Interestingly, during the course of the MD simulations of VAP-1 with the bound ligand **5a** (Table 1), which is considerably larger than 2-hydrazinopyridine as seen in the crystal structure, the side chain of Leu469 rotates and unblocks the ligand-binding cavity, providing ligands with free access from the solvent to the ligand-binding pocket (Figure 2C,D). This new conformation of Leu469 is stabilized by hydrophobic interactions with Phe239 (Figure 2D). Another remarkable conformational change observed in MD simulations is that the side chains of Met211 and Ser496 rotate, and additional space becomes available for ligand binding (Figure 2B,D); however, none of inhibitors in

Table 1. Structures of the Synthesized Hydrazine Molecules and Commercially Available Phenelzine, and Their Measured Biological Potency, Predicted pIC_{50} Values for Both VAP-1 and MAO as Well As the Selectivity of VAP-1 over MAO

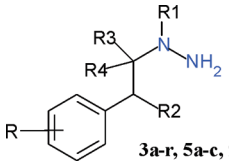

3a-r, 5a-c, 9a-j, 10a-d and **12a-j**

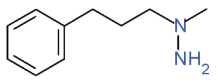

3s

molecule	R	R1	R2	R3	R4	VAP1 $pIC_{50} \pm pSEM$[a] pred. pIC_{50}[b]	MAO $pIC_{50} \pm pSEM$[a] pred. pIC_{50}[b]	selectivity IC_{50}[c] pred. IC_{50}[d]
phenelzine[g]	H	H	H	H	H	7.70 ± 0.22	6.15 ± 0.06	40
						7.38	6.11	20
3a	H	CH_3	H	H	H	6.96 ± 0.04	5.27 ± 0.06	50
						6.70	4.58	130
3b	2-F	CH_3	H	H	H	7.04 ± 0.05	5.41 ± 0.07	40
						7.10	5.74	23
3c	4-F	CH_3	H	H	H	6.96 ± 0.12	5.64 ± 0.11	21
						7.13	5.70	27
3d	2-Cl	CH_3	H	H	H	6.77 ± 0.08	5.43 ± 0.14	22
						6.94	5.51	27
3e	3-Cl	CH_3	H	H	H	6.92 ± 0.11	5.48 ± 0.08	28
						6.92	5.54	24
3f	4-Cl	CH_3	H	H	H	7.15 ± 0.06	5.50 ± 0.09	50
						7.09	5.74	22
3g	2-OCH_3	CH_3	H	H	H	6.46 ± 0.05	5.22 ± 0.12	17
						6.48	5.11	23
3h	3-OCH_3	CH_3	H	H	H	7.05 ± 0.05	5.70 ± 0.22	20
						6.95	5.34	40
3i	4-OCH_3	CH_3	H	H	H	7.22 ± 0.07	5.68 ± 0.17	40
						7.15	5.36	60
3j	2,5-$(OCH_3)_2$	CH_3	H	H	H	6.43 ± 0.06	5.41 ± 0.07	11
						6.23	5.19	11
3k	3,4-$(OCH_3)_2$	CH_3	H	H	H	6.46 ± 0.06	5.20 ± 0.07	18
						6.70	5.22	30
3l	2,3,4-$(OCH_3)_3$	CH_3	H	H	H	6.48 ± 0.07	4.96 ± 0.16	33
						6.37	4.92	28
3m	3,4,5-$(OCH_3)_3$	CH_3	H	H	H	6.49 ± 0.05	4.64 ± 0.09	72
						6.30	5.08	17
3n	H	CH_2CH_3	H	H	H	6.74 ± 0.02	5.74 ± 0.04	10
						6.68	5.48	16
3o	4-OCH_3	CH_2CH_3	H	H	H	7.10 ± 0.11	5.46 ± 0.16	40
						6.87	5.55	20
3p	3,4,5-$(OCH_3)_3$	CH_2CH_3	H	H	H	5.65 ± 0.09	4.89 ± 0.07	6
						5.78	5.17	4
3q	H	$CH_2CH(CH_3)_2$	H	H	H	6.36 ± 0.03	5.47 ± 0.02	8
						6.65	5.62	11
3r	4-OCH_3	$CH_2CH(CH_3)_2$	H	H	H	6.59 ± 0.05	5.57 ± 0.31	10
						6.67	5.55	13
3s						6.62 ± 0.14	5.41 ± 0.16	16
						6.59	5.59	10
5a	H	H	OH	H	H	7.19 ± 0.01	5.05 ± 0.05	140
						7.18	5.27	80
5b	3-OCH_3	H	OH	H	H	7.28 ± 0.08	5.04 ± 0.02	200
						7.28	5.17	130
5c	4-OCH_3	H	OH	H	H	7.54 ± 0.15	5.22 ± 0.00	200
						7.28	5.19	120
9a	H	CH_3	OH	H	H	6.68 ± 0.04	4.40 ± 0.01	190
						6.72	4.57	140
9b	2-Cl	CH_3	OH	H	H	6.57 ± 0.08	4.64 ± 0.02	85
						6.69	4.63	120
9c	4-Cl	CH_3	OH	H	H	6.51 ± 0.04	4.68 ± 0.02	68
						6.64	4.61	110
9d	3-OCH_3	CH_3	OH	H	H	6.55 ± 0.05	4.36 ± 0.02	160
						6.69	4.51	150
9e	4-OCH_3	CH_3	OH	H	H	6.51 ± 0.03	4.44 ± 0.05	120
						6.74	4.49	180
9f	4-F	CH_3	OH	H	H	6.49 ± 0.07	4.42 ± 0.01	120
						6.72	4.59	140

Table 1. Continued

molecule	R	R1	R2	R3	R4	VAP1 $pIC_{50} \pm pSEM$[a] pred. pIC_{50}[b]	MAO $pIC_{50} \pm pSEM$[a] pred. pIC_{50}[b]	selectivity IC_{50}[c] pred. IC_{50}[d]
9g	2,3,4-$(OCH_3)_3$	CH_3	OH	H	H	6.66 ± 0.04	4.35 ± 0.02	200
						6.58	4.52	120
9h	3,4-[$O(CH_2)_2O$]	CH_3	OH	H	H	6.70 ± 0.07	4.55 ± 0.03	140
						6.70	4.32	240
9i	2-naphthyl[e]	CH_3	OH	H	H	6.37 ± 0.02	4.64 ± 0.04	53
						6.31	4.65	46
9j	H	$CH_2CH(CH_3)_2$	OH	H	H	6.46 ± 0.04	4.96 ± 0.08	31
						6.39	4.91	30
10a[f]	H	CH_3	OH	CH_3	H	6.46 ± 0.14	4.41 ± 0.02	110
						6.29	4.50	62
10b[f]	H	CH_3	OH	CH_2CH_3	H	6.59 ± 0.10	4.39 ± 0.03	160
						6.35	4.19	150
10c[f]	H	CH_3	OH	$(CH_2)_2CH_3$	H	6.59 ± 0.07	4.55 ± 0.02	110
						6.47	4.70	60
10d	H	CH_3	OH	CH_3	CH_3	6.25 ± 0.05	4.26 ± 0.02	100
						6.70	4.65	110
12a	3-F	CH_3	OCH_3	H	H	6.36 ± 0.02	4.69 ± 0.02	47
						6.58	4.56	110
12b	4-F	CH_3	OCH_3	H	H	6.24 ± 0.04	4.51 ± 0.01	53
						6.21	4.35	72
12c	3-Cl	CH_3	OCH_3	H	H	6.39 ± 0.04	4.77 ± 0.10	41
						6.39	4.41	95
12d	4-Cl	CH_3	OCH_3	H	H	6.37 ± 0.04	4.72 ± 0.04	44
						6.16	4.26	80
12e	3-CH_3	CH_3	OCH_3	H	H	6.49 ± 0.04	4.47 ± 0.08	110
						6.35	4.65	50
12f	3-OCH_3	CH_3	OCH_3	H	H	6.39 ± 0.01	4.36 ± 0.01	110
						6.45	4.63	70
12g	4-OCH_3	CH_3	OCH_3	H	H	6.38 ± 0.03	4.36 ± 0.01	110
						6.35	4.61	60
12h	2,3,4-$(OCH_3)_3$	CH_3	OCH_3	H	H	6.20 ± 0.03	4.15 ± 0.01	110
						6.29	4.68	40
12i	1-naphthyl[e]	CH_3	OCH_3	H	H	6.40 ± 0.03	4.57 ± 0.16	68
						6.34	4.58	58
12j	2-naphthyl[e]	CH_3	OCH_3	H	H	6.64 ± 0.04	4.88 ± 0.07	57
						6.62	4.67	89

[a] Experimental pIC_{50} data in M concentration. The pIC_{50}-errors (for 2−4 similar experiments) are given as a relative error (SEM/IC_{50})*0.434 that results significant progressive error with large IC_{50}-errors. [b] Predicted pIC_{50} values (final 3D QSAR models; see Table 2). [c] Selectivity of molecules from IC_{50}-data MAO over VAP-1 [IC_{50}(MAO)]/[IC_{50}(VAP-1)]. [d] Predicted selectivity calculated from the pIC_{50}-values $10^{[\text{predicted pIC50 (VAP-1)-predicted pIC50 (MAO)}]}$. [e] 1-Naphtyl or 2-naphtyl group instead of phenyl group, does not refer to R. [f] Relative configuration 1*R**,2*S**; 1*R**,2*S**; 1*R**,2*S**. [g] Commercially available.

Scheme 1[a]

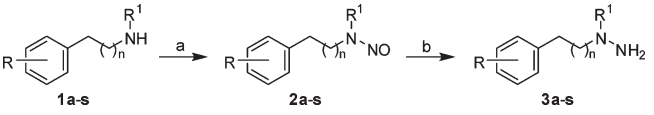

[a] Reagents: (a) $NaNO_2$, AcOH, H_2O; (b) $LiAlH_4$, THF (for the meaning of R, R^1, and n see Table 1).

Scheme 2[a]

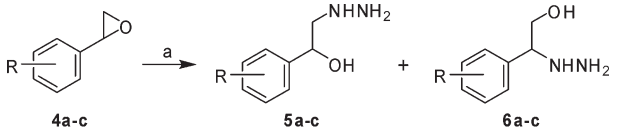

R = H: **a**, 3-OCH_3: **b**, 4-OCH_3: **c**

[a] Reagents: (a) $H_2NNH_2 \cdot H_2O$, EtOH.

Scheme 3[a]

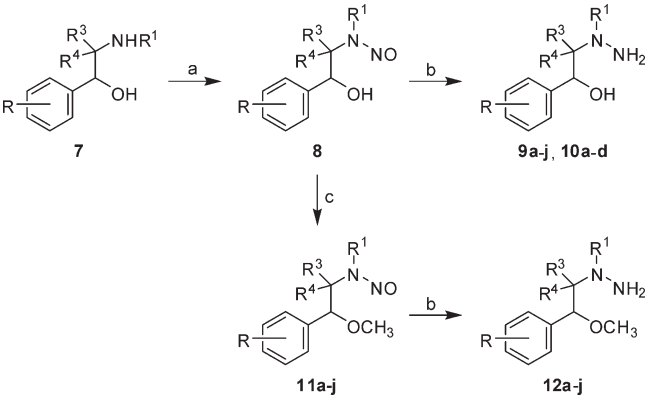

[a] Reagents: (a) $NaNO_2$, AcOH, H_2O; (b) $LiAlH_4$, THF; (c) NaH, MeI, THF (for the meaning of R, R^1, R^3, and R^4 see Table 2).

this study seem to use this additionally available space. However, the site could be very important for VAP-1 selectivity over total MAOs and should be taken into account when new VAP-1 selective molecules are designed. None of the

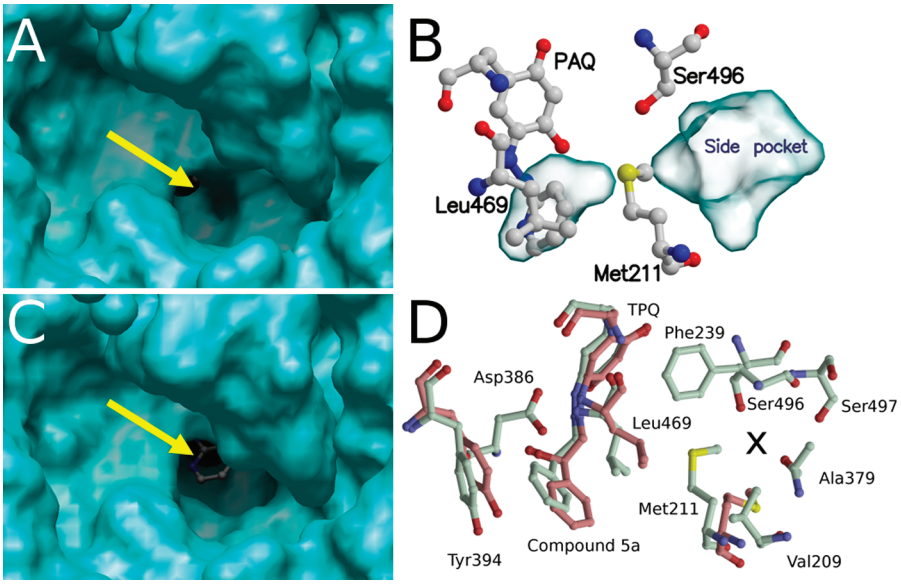

Figure 2. Flexibility of VAP-1 ligand binding site (A) Leu469 acts as a gate residue that blocks the entry into substrate binding site; (B) in the crystal structure of VAP-1 with bound 2-hydrazinopyridine amino acids Met211 and Ser496 form a wall to the substrate binding site that separates the substrate binding site and much larger side pocket. (C) Ligands can enter into substrate binding site, when the gate residue Leu469 takes another conformation. (D) During the MD simulation of VAP-1 with bound **5a** the gate residue Leu469 is held "open" and Met211 and Ser496 rotate and reveal a direct entrance from substrate binding site into side pocket (marked with X). In (A) and (C) the entrance into substrate binding site is pointed with a yellow arrow. In (D) the starting structure (light green carbon atoms) and the key conformational changes (pink carbon atoms) are shown.

Table 2. Statistics of 3D QSAR Models

model (protein)	q^2_{LOO}	r^2	SEE[a]	no. of components	q^2_{pred}[b]	q^{**2}[c]	cSDEP[c]	$dq^{2'}/dr^2_{yy}$[c]	q^2_{bs}[d]
submodel 1 (VAP-1)	0.602	0.804	0.150	3	0.63				
submodel 2 (VAP-1)	0.522	0.855	0.162	4	0.66				
submodel 3 (VAP-1)	0.623	0.881	0.141	4	0.50				
submodel 4 (VAP-1)	0.601	0.861	0.157	4	0.58				
final model (VAP-1)	*0.636*	*0.828*	*0.163*	*4*		*0.5457*	*0.2664*	*0.3373*	*0.868*
submodel 1 (MAO)	0.676	0.838	0.208	3	0.79				
submodel 2 (MAO)	0.717	0.843	0.205	3	0.63				
submodel 3 (MAO)	0.776	0.866	0.200	2	0.53				
submodel 4 (MAO)	0.673	0.824	0.223	3	0.88				
final model (MAO)	*0.749*	*0.840*	*0.209*	*3*		*0.5661*	*0.3612*	*0.9379*	*0.880*

[a] Standard error of estimate. [b] q^2_{pred} value acquired from the prediction of the molecules in test set (Table S1, column Set). [c] Model validation with progressive scrambling-method. [d] Model validation with bootstrapping-method.

other amino acids of the VAP-1 ligand-binding pocket undergo any noteworthy conformational changes. Taken together, these simulations clearly reveal that ligands having considerably larger substituents at position R1 than hydrogen, as seen in **5a** (Table 1), could also bind to VAP-1. This information is valuable for designing more selective and better inhibitors for VAP-1.

3D QSAR Model Building. To fully understand the relationship between the ligand structure and its associated biological activity, we used the 3D QSAR technique to build statistical models that could explain and predict the binding affinities for synthesized hydrazines. The superpositioning of the ligands for 3D QSAR was obtained by using molecular docking into the crystal structure of VAP-1,[11] where the conformation of Leu469 was changed to resemble that seen in MD simulations. The representative conformation for each ligand was selected based on the fitness function implemented in the docking software. The molecules were divided into four subsets, out of which three were used to build the model and one was used as a test set (see Supporting Information: Table S1, column: set), in order to validate the built models for a full ligand set (four submodels, Table 2). These validation sets resulted in a final model that predicted the potency of test set molecules with reasonable accuracy (Figure 3; Table 2: q^2_{pred}). All 47 molecules were also predicted using final models (Table 2). All 47 molecules fit into the final 3D QSAR models; that is, no outliers were detected (Figure 3). Accordingly, this model should yield predictions with even higher reliability than those of the submodels. The final comparative molecular similarity indices analysis (CoMSIA) models were built by using leave one out (LOO) cross-validation (Table 2). The QSAR model for total MAO was constructed using the ligand superposition obtained from the docking simulations to VAP-1. Similarly as for VAP-1, four submodels and a final model were also built for MAO (Table 2). Accordingly, single-ligand superpositioning can be used to obtain meaningful predictions for both VAP-1 and MAOs. For the VAP-1 3D QSAR model, the correlation coefficients q^2_{LOO}, r^2 0.636, and 0.828, respectively, were obtained by means of a steric CoMSIA field (Table 2). Four partial least-squares (PLS) components were used and the standard error of estimate (SEE) value was 0.163 (Table 2). For the MAO 3D QSAR model, the best correlation was found with the hydrophobic

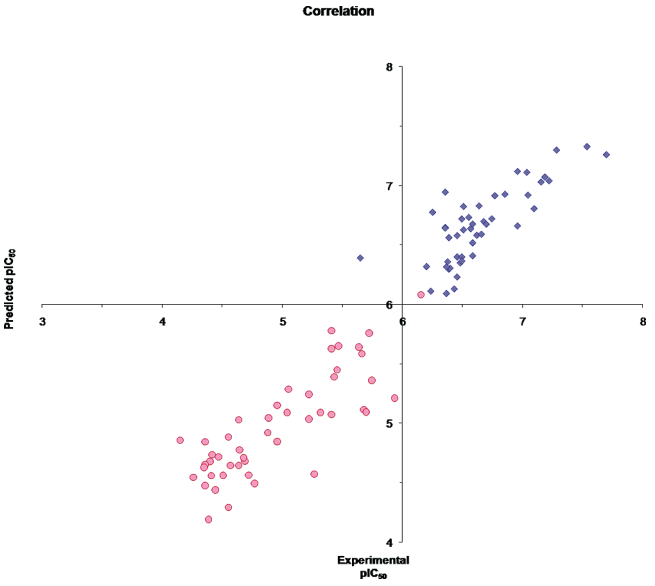

Figure 3. Correlation between the experimental and predictions of submodels −log IC_{50}. Blue squares represent VAP-1 correlation, red spots MAO correlation.

field (q^2_{LOO}: 0.749; r^2: 0.840), where three PLS components was used, and the SEE was 0.209 (Table 2). With neither of the enzymes, other CoMSIA fields did not have as good correlations with the experimental data. For example, the hydrophobic field for VAP-1 and the steric field for total MAO also correlated (see Supporting Information Table S2), but especially q^2_{LOO} values were lower than the steric field for VAP-1 and the hydrophobic field for total MAO, respectively (Table 2). Combining the steric and electrostatic field, in turn, correlated for both VAP-1 and MAO, but with an outlier (see Supporting Information in Table S2 and Figure S1).

Numerically both of the developed 3D QSAR models indicate that the IC_{50}-values for similar molecules can be predicted with reasonable accuracy, and they should be able to separate the active inhibitors from inactive molecules. For example, the predictions made using submodels (Figure 3) show that the predicted potencies are clearly within one log-unit of those experimentally measured. In practice, for both VAP-1 and total MAO, the range of inhibitor potencies is fairly narrow to build a quantitative QSAR model: approximately two logarithmic units. Thus, the inhibitor potency predictions cannot be reliably made outside this potency range. Furthermore, because of the redundancy in the data set, further validation of the models was done by employing progressive scrambling[45] and bootstrapping methods.[46,47] These data show that the models are resilient to chance (Table 2: $dq^{2'}/dr^2_{yy}$-values are lower than one), as well as being predictive (Table 2).

Interpretation of Molecular Fields Using in Vitro Data. The advantage of using enzyme structure-based inhibitor overlay in 3D QSAR rather than superposition based on ligand structures alone is that the molecular fields can be visualized within the inhibitor binding site. This allows for the evaluation of the reasonableness of the developed 3D QSAR model by analyzing the possible interaction sites between the inhibitors and the amino acids at the binding cavity. As the VAP-1 data correlates with the steric CoMSIA field, the areas of favorable steric fields have space that could be filled by the ligand's substituents. According to the proposed covalent mechanism of inhibition, IC_{50}-values include association, reactivity, and dissociation components. In the case of MAO, the hydrazine molecules react with flavin adenine dinucleotide[34] most likely via the mechanism where dissociation of the $N(R1)NH_2$ moiety leads to the same covalently bound products if the remaining substitution patterns are identical (e.g., in the case of **phenelzine**, **3a**, **3n**, and **3q**). However, in case of VAP-1 the hydrazine moiety remains in the covalently bound product.[10] These different components of binding affinity should also affect the QSAR models. Accordingly, reaction ability especially influences the molecular fields near the hydrazine-moiety in both VAP-1 and MAO. For example, there are unfavorable fields in VAP-1 (steric: Figure 4A, yellow) and total MAO (hydrophobic: Figure 4B, red) 3D QSAR models adjacent to the hydrazine moiety, which implies that substituents larger than hydrogen atoms at position R1 would be disadvantageous for both VAP-1 and MAO inhibition (Table 1). This can also be seen from the experimental data when, for example, **phenelzine**, **3a**, **3n**, and **3q**, or **5a**, **9a**, and **9j** are compared (Table 1). However, if the size of the R1-groups exceeds that of the methyl-group, the selectivity toward VAP-1 against MAO is decreased dramatically (e.g., compare compounds **3a** and **3n**, **3q**, and **9a** and **9j**: Table 1).

The hydroxyl group at position R2 decreases both VAP-1 and MAO potency (compare e.g., **phenelzine-5a**, **3a**−**9a**, **3d**−**9b**, **3f**−**9c**, **3h-9d**, **3i**−**9e**) except in compounds where the aryl group has a fluoro group at the para-position (**9f**−**12b**), or there is 2-naphtyl in place of the benzene ring (**9i**−**12j**). Also, when the aryl group is trisubstituated (2,3,4-$(OCH_3)_3$, **3l**, **9g**), the addition of the hydroxyl group decreases MAO potency but increases slightly VAP-1 potency. In those molecules, where the addition of the hydroxyl group at position R2 decreases both VAP-1 and MAO potency, the influence is more prominent with MAO and, consequently, the VAP-1 selectivity over MAO is clearly improved. Actually, the molecules containing a hydroxyl-group at position R2 are the most selective inhibitors in the molecule set (Table 1). Modification of the R2 hydroxyl-group to a methoxy-group does not have any clear influence on either VAP-1 or MAO potency (Table 1).

Addition of substituents to positions R3 and R4 (compare **9a** and **10a**−**d**) has only a modest effect on MAO inhibitory potency but slightly decreases VAP-1 potency, which clearly decreases VAP-1 selectivity over MAO, especially when both R3 and R4 positions are substituted (**10d**: Table 1).

The second favorable steric field (Figure 4A,C, green II) shows that the addition of R-substituents to the para-position (R-group, Table 1) of the phenyl ring improves the binding to VAP-1. This is logical, as this area is toward the VAP-1 surface. This is consistent with the inhibition data as well. For example, with the addition of the methoxy-group at the para-position of compounds **3a** and **5a**, resulting in compounds **3i** and **5c**, respectively, the inhibition of VAP-1 is slightly increased. However, if the R1-substituent is the methyl-group instead of the hydrogen atom, the VAP-1 inhibition ability is decreased when a methoxy-group is added to the para-position of the phenyl ring (compare **9a** and **9e**, Table 1). The influence of the para-substitutions to selectivity is complex; when R2 is the hydroxyl-group rather than the hydrogen atom, the VAP-1 selectivity over MAO is increased (**3a**−**3i**, **5a**−**5c**).

In addition to the favorable steric field near the phenyl group, two sterically unfavorable fields are also found in the

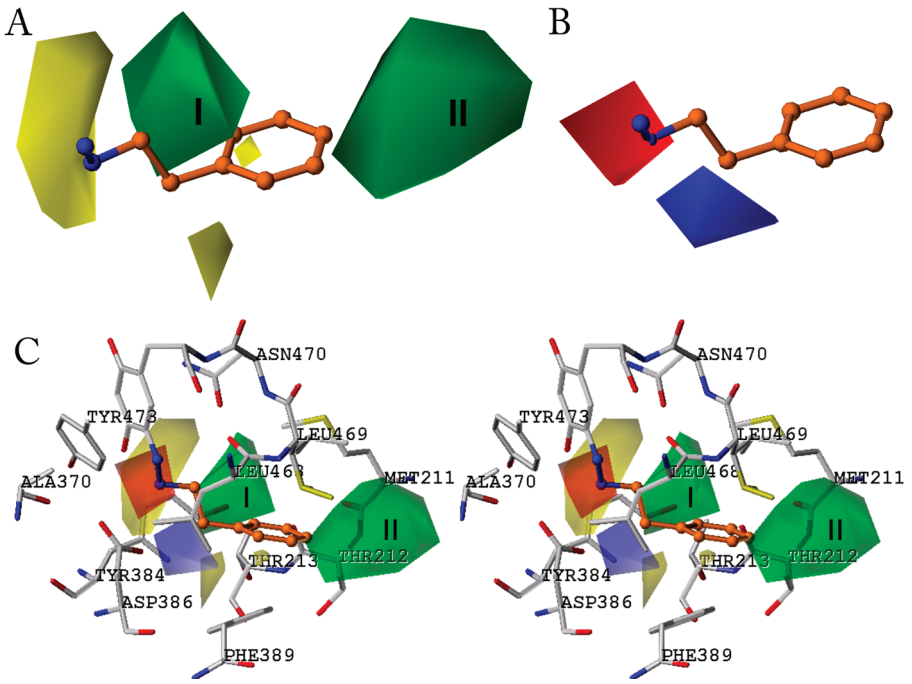

Figure 4. CoMSIA fields and the reference molecule (phenelzine, Table 1). (A) CoMSIA fields for VAP-1. Sterically favorable areas are green and unfavorable areas yellow and they are shown with contribution levels of 85% and 25%, respectively. (B) CoMSIA fields for MAO. Hydrophobically favorable areas are blue and unfavorable areas are red, and they are shown with contribution levels of 80% and 15%, respectively. In (C), the parallel stereoview of the same spatial distribution of the CoMSIA fields in the ligand binding pocket.

VAP-1 3D QSAR model (Figure 4A,C: small yellow areas). The clearest effect is seen with the compound **9i**, where the phenyl group is replaced by 2-naphtyl and the VAP-1 inhibition potency is clearly decreased compared to that of the parent compound **9a**.

Overall, the fields from the 3D QSAR model of MAO (Figure 4B) are obviously more difficult to rationalize, as the model is based on ligand superposition obtained from a docking experiment to the VAP-1 structure. However, this ligand-based alignment delineates the effect of field variables on potency and leads to a descriptive and predictive QSAR model. In particular, the location of MAO fields around the ligand can be used to analyze where hydrophobic groups would be beneficial for MAO but not necessarily for VAP-1. Thus, these MAO-favorable fields can be used to guide the synthesis of VAP-1 inhibitors in a way that favorable sites for MAO inhibition would be avoided, especially if they do not simultaneously contribute toward VAP-1 binding. Comparison of the favored and unfavorable fields of MAO and VAP-1 shows an interesting area where the hydrophobically favorable field of MAO and the sterically unfavorable field of VAP-1 overlap, in the area between the ligand and Phe389 (Figure 4). This MAO-favoring region can also be seen by comparing the selectivity of compound-series **9** and **12** (Table 1), where the methylation of hydroxyl-group (R2-substitution) decreases the binding into VAP-1 (except in the compound pair **9i** and **12j**, where the aryl group is 2-naphtyl), while the MAO potency is generally not affected. Thus, the selectivity is lowered 2−3 times (Table 1). Accordingly, addition of a group at this position should be avoided, since it reduces VAP-1 selectivity.

Prediction, Synthesis, and in Vitro Potency of Novel Ligands. To further validate the built 3D QSAR models, they were used to predict the IC_{50} values for hydrazine molecules that have novel features, in contrast to those used in the model building (Table 1). Specifically, we wanted to challenge our 3D QSAR models with molecules whose properties vary significantly from those compounds that were used in the model development. On the basis of predicted inhibitor potency and selectivity toward VAP-1 over MAO, three molecules were synthesized (Table 3: **13**, **15**, **16**). Also, two molecules with less selectivity were synthesized, since they have novel substituents (Table 2: **14a**, **14b**). Compounds **13**−**16** were synthesized similarly to the analogous derivatives **3**, **9**, and **12.** In general, the developed molecules were predicted to be slightly better inhibitors of VAP-1 than they actually are, while the MAO potency was predicted quite accurately (Table 3). First, we predicted a compound that has a shorter linker between the hydrazine moiety and the phenyl ring, that is, only one CH_2-group in between (Table 3: **13**). This was very challenging for the 3D QSAR models, as they do not contain any molecules with such a short link. This compound **13** was predicted to be highly active and selective (pIC_{50}-values for VAP-1: 7.70; MAO: 5.32, Table 3); however, the measured IC_{50} values (pIC_{50}-values for VAP-1: 6.57; MAO: 5.74, Table 3) show that the models cannot reliably predict this type of compound. Second, as the VAP-1 3D QSAR model was built by using a steric field that cannot discriminate between polar and hydrophobic groups, we challenged the VAP-1 3D QSAR model by developing molecules **14a** and **14b**, which have a methyl group at position 2, instead of the hydroxyl group seen in their counterpart compounds **5a** and **9a**, respectively. Logically, the predicted pIC_{50} values for these two new compounds should be more highly similar than for their counterparts (**14a**: 7.41; **5a**: 7.19; **14b**: 6.67; **9a**: 6.68, Tables 1 and 3). It is noteworthy that the measured pIC_{50}-values are also quite similar to those predicted (**14a**: 7.23; **14b**: 6.33 μM; Table 3). When both the hydroxyl and methyl group were introduced into position 2 of the ligand (**15**), both 3D QSAR models

Table 3. Structures of Five Novel Hydrazines and Their Predicted and Measured pIC_{50} Values for the Inhibition of VAP-1 and MAO

Compound	Predicted VAP-1 pIC_{50} M	Predicted MAO pIC_{50} M	Measured VAP-1 pIC_{50} M [a]	Measured MAO pIC_{50} M [b]
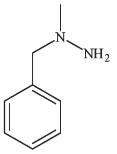 **13**	7.70	5.32	6.57	5.74
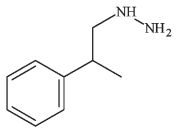 **14a**	7.41	5.95	7.23±0.14	6.46±0.02
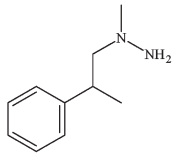 **14b**	6.67	5.67	6.33±0.05	5.26±0.08
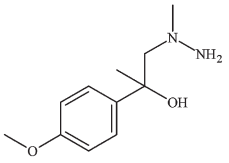 **15**	7.18	4.63	6.46±0.06	3.96±0.06
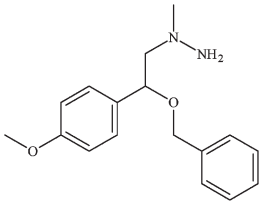 **16**	7.02	4.83	6.41±0.08	4.60±0.14

[a] pIC_{50} data for VAP-1 in M concentration, mean ± pSEM of 2−4 similar experiments [pSEM = (SEM/IC_{50})*0.434]. [b] pIC_{50} data for MAO in M concentration, mean ± pSEM of 2−4 similar experiments.

slightly overestimated the binding (VAP-1:0.72 log-units; MAO: 0.67 log-units: Table 3). This is quite a small error in the context that none of the original compounds contained two substituents in position 2. What is notable for future ligand discovery is that compound **15** uses both sterically favored regions in VAP-1 3D QSAR models (fields shown in Figure 4A), which also resulted in high selectivity of this compound (2.5 log-units, i.e., >300-fold selectivity to VAP-1 over MAO, Table 3). Finally, we introduced a clearly larger substituent into ligand position 2 (**16**; Table 3). Again, the 3D QSAR models should not be able to predict this compound accurately, as none of the compounds used in the 3D QSAR model building had such a large substituent in position 2. However, the predictions were surprisingly good, and also this compound shows selectivity toward VAP-1 against MAO (1.8 log-units: Table 3).

The model presented here is the first published 3D QSAR model for VAP-1 inhibitors, although structure−activity relationship studies for SSAO substrates[43,44] and 3D QSAR study for MAO A inhibitors[32] have been published previously. The models obtained in this study are excellent tools to guide future inhibitor discovery toward more potent and selective ligands for VAP-1. The statistics (Table 2) suggest that when using 3D QSAR models to predict potencies for unmeasured molecules, these models can sufficiently predict IC_{50} values. The molecules that have functional groups at the positions that have not been varied within this ligand series are beyond the limits of these models and cannot therefore be predicted reliably. However, as shown for five molecules that do not fall into same ligand set, the predictions can be quite accurate (Table 3). In addition to direct usage of these 3D QSAR models in the prediction of new molecules, the developed 3D QSAR model can indicate which properties are favorable for the design of ligands, no matter whether they are similar to these covalently binding hydrazines, or designed to bind reversibly. The binding mode of possible reversible ligands is not yet known, so the descriptor fields near TPQ should be ignored, since the orientation of TPQ could be either oxidized (inactive, bound to the copper ion[11]) or reduced (active,[10] also used in this study).

Conclusions

A series of hydrazine compounds has been synthesized and shown to selectively inhibit VAP-1 activity over MAO. The built 3D QSAR model for VAP-1 is based on a rather large set of biologically tested molecules (47 molecules) and can hence be considered to be rather accurate for the prediction of the properties required for selective and effective VAP-1 inhibitors. Combination of the data from the 3D QSAR model with the results obtained from MD simulations allows for the design of even better inhibitors with different scaffolds. However, when reversible inhibitors are developed, it must be kept in mind that the TPQ can be in both inactive and active conformations, and accordingly the 3D QSAR fields near the TPQ should be used with care.

Materials and Methods

Materials. Benzylamine, tyramine, 2,4-dichlorophenol, 4-aminoantipyrine, and horseradish peroxidase were purchased from Sigma (St. Louis, MO). Cell culture reagents were supplied by Gibco. Other chemicals were of analytical or reagent grade, and were purchased from commercial suppliers.

Methods. Synthesis. General Methods. Melting points were measured on a Kofler hot-plate microscope apparatus and are uncorrected. For routine thin-layer chromatography (TLC), Silica gel 60 F_{254} plates (Merck, Germany) were used. Elemental analyses were performed with a Perkin-Elmer 2400 CHNS elemental analyzer. ^{1}H NMR spectra were recorded in $CDCl_3$, in DMSO-d_6 or in D_2O solutions on a Bruker DRX 400 or DRX 500 spectrometer by using completely dissolved samples. These spectra indicated the >95% purities of the prepared compounds. Chemical shifts are given in δ (ppm) relative to TMS ($CDCl_3$, DMSO-d_6) or to TSP (D_2O) as internal standards.

General Procedure for the Preparation of N-Nitroso Amines 2 and Amino Alcohols 8. A solution of $NaNO_2$ (1.38 g, 20 mmol) in H_2O (5 mL) was added dropwise to a suspension/emulsion/solution of the corresponding amine (**1a**−**s**) or amino alcohol (**7**) (10 mmol) in H_2O (20 mL) with vigorous stirring on an ice-cold bath, and then AcOH (0.90 g, 15 mmol) was added dropwise. The mixture was stirred at room temperature for 5−10 h and then was extracted with EtOAc (4 × 30 mL). The combined organic phases were dried (Na_2SO_4) and evaporated under reduced pressure to give the *N*-nitroso derivative which was used in the next steps without further purification.

General Procedure for the Preparation of Hydrazines 3a−s, 13, and 14b and Hydrazino Alcohols 9a−j and 10a−d and 15. A solution of the corresponding *N*-nitroso compound (**2** or **8**, 10 mmol) in THF (10 mL) was added dropwise to a stirred and ice-cooled suspension of $LiAlH_4$ (0.76 g, 20 mmol) in THF (25 mL), and the mixture was stirred at ambient temperature for 3 h. The excess of $LiAlH_4$ was decomposed with a mixture of H_2O (1.5 mL) and THF (20 mL), and the resulting precipitate was filtered off and washed with EtOAc (3 × 25 mL). The combined filtrate and washings were dried (Na_2SO_4) and evaporated under reduced pressure. The oily residue was treated with an equivalent amount of maleic or fumaric acid, or with an excess of 22% ethanolic HCl in a mixture of EtOH and Et_2O to give crystalline salts which was filtered off and recrystallized.

1-Methyl-1-(2-phenylethyl)hydrazine Hydrochloride (3a Hydrochloride). White crystalline solid, yield 1.18 g (63%); mp 93−94 °C (EtOH−Et_2O); ^{1}H NMR (400 MHz, D_2O) δ 3.06 (s, 3H, NCH_3), 3.07−3.14 (m, 2H, ArCH_2), 3.48−3.55 (m, 2H, NCH_2), 7.31−7.46 (m, 5H, C_6H_5). Anal. Calcd for $C_9H_{15}ClN_2$: C, 57.90; H, 8.10; N, 15.04. Found: C, 57.63; H, 7.98; N, 14.88.

1-[2-(2-Fluorophenyl)ethyl]-1-methylhydrazine Hydrochloride (3b Hydrochloride). White crystalline solid, yield 1.66 g (81%); mp 138−140 °C (EtOH−Et_2O); ^{1}H NMR (400 MHz, D_2O) δ 3.06 (s, 3H, NCH_3), 3.11−3.18 (m, 2H, ArCH_2), 3.47−3.53 (m, 2H, NCH_2), 7.15−7.25 (m, 2H, C_6H_4), 7.34−7.41 (m, 2H, C_6H_4). Anal. Calcd for $C_9H_{14}ClFN_2$: C, 52.81; H, 6.89; N, 13.69. Found: C, 52.54; H, 6.61; N, 13.48.

1-[2-(4-Fluorophenyl)ethyl]-1-methylhydrazine Hydrogen Maleate (3c Hydrogen Maleate). White crystalline solid, yield 1.96 g (69%); mp 82−84 °C (EtOH−Et_2O); ^{1}H NMR (400 MHz, D_2O) δ 3.04−3.12 (m, 5H, NCH_3, ArCH_2), 3.47−3.54 (m, 2H, NCH_2), 6.28 (s, 2H, CH=CH), 7.09−7.17 (m, 2H, C_6H_4), 7.29−7.37 (m, 2H, C_6H_4). Anal. Calcd for $C_{13}H_{17}FN_2O_4$: C, 54.92; H, 6.03; N, 9.85. Found: C, 54.66; H, 5.83; N, 9.72.

1-[2-(2-Chlorophenyl)ethyl]-1-methylhydrazine Hydrochloride (3d Hydrochloride). Beige crystalline solid, yield 1.62 g (73%); mp 97−99 °C (EtOH−Et_2O); ^{1}H NMR (400 MHz, D_2O) δ 3.08 (s, 3H, NCH_3), 3.20−3.26 (m, 2H, ArCH_2), 3.45−3.52 (m, 2H, NCH_2), 7.31−7.44 (m, 3H, C_6H_4), 7.47−7.53 (m, 1H, C_6H_4). Anal. Calcd for $C_9H_{14}Cl_2N_2$: C, 48.88; H, 6.38; N, 12.67. Found: C, 48.60; H, 6.29; N, 12.55.

1-[2-(3-Chlorophenyl)ethyl]-1-methylhydrazine Hydrochloride (3e Hydrochloride). Yellowish white crystalline solid, yield 1.65 g (75%); mp 73−76 °C (EtOAc−Et_2O); ^{1}H NMR (400 MHz, D_2O) δ 3.02−3.13 (m, 5H, ArCH_2, NCH_3), 3.46−3.54 (m, 2H, NCH_2), 7.25−7.31 (m, 1H, C_6H_4), 7.34−7.43 (m, 3H, C_6H_4). Anal. Calcd for $C_9H_{14}Cl_2N_2$: C, 48.88; H, 6.38; N, 12.67. Found: C, 49.02; H, 6.25; N, 12.51.

1-[2-(4-Chlorophenyl)ethyl]-1-methylhydrazine Hydrochloride (3f Hydrochloride). Pale yellow crystalline solid, yield 1.72 g (78%); mp 96−98 °C (EtOH−Et_2O); ^{1}H NMR (400 MHz, D_2O) δ 3.02−3.12 (m, 5H, ArCH_2, NCH_3), 3.46−3.53 (m, 2H, NCH_2), 7.32 (d, 2H, J = 8.3 Hz, C_6H_4), 7.42 (d, 2H, J = 8.3 Hz, C_6H_4). Anal. Calcd for $C_9H_{14}Cl_2N_2$: C, 48.88; H, 6.38; N, 12.67. Found: C, 48.69; H, 6.46; N, 12.63.

1-[2-(2-Methoxyphenyl)ethyl]-1-methylhydrazine Hydrogen Maleate (3g Hydrogen Maleate). Beige crystalline solid, yield 1.68 g (57%); mp 61−63 °C (EtOH−Et_2O); ^{1}H NMR (400 MHz, DMSO-d_6) δ 2.50 (s, 3H, NCH_3) 2.78−2.90 (m, 2H, ArCH_2), 2.99−3.12 (m, 2H, NCH_2), 3.80 (s, 3H, OCH_3), 6.03 (s, 2H, CH=CH), 6.87−7.03 (m, 2H, C_6H_4), 7.15−7.30 (m, 2H, C_6H_4). Anal. Calcd for $C_{14}H_{20}N_2O_5$: C, 56.75; H, 6.80; N, 9.45. Found: C, 56.62; H, 6.97; N, 9.41.

1-[2-(3-Methoxyphenyl)ethyl]-1-methylhydrazine Hydrogen Maleate (3h Hydrogen Maleate). Beige crystalline solid, yield 1.84 g (62%); mp 88−90 °C (EtOH−Et_2O); ^{1}H NMR (400 MHz, D_2O) δ 3.03−3.14 (m, 5H, NCH_3, ArCH_2), 3.48−3.57 (m, 2H, NCH_2), 3.84 (s, 3H, OCH_3), 6.28 (s, 2H, CH=CH), 6.93−7.02 (m, 3H, C_6H_4), 7.33−7.40 (m, 1H, C_6H_4). Anal. Calcd for $C_{14}H_{20}N_2O_5$: C, 56.75; H, 6.80; N, 9.45. Found: C, 56.55; H, 6.69; N, 9.54.

1-[2-(4-Methoxyphenyl)ethyl]-1-methylhydrazine Hydrogen Maleate (3i Hydrogen Maleate). White crystalline substance, yield 1.90 g (64%); mp 113−115 °C (EtOH−Et_2O); ^{1}H NMR (400 MHz, D_2O) δ 3.00−3.08 (m, 5H, ArCH_2, NCH_3), 3.45−3.52 (m, 2H, NCH_2), 3.82 (s, 3H, OCH_3), 6.27 (s, 2H, CH=CH), 6.99 (d, 2H, J = 8.6 Hz, C_6H_4), 7.28 (d, 2H, J = 8.6 Hz, C_6H_4). Anal. Calcd for $C_{14}H_{20}N_2O_5$: C, 56.75; H, 6.80; N, 9.45. Found: C, 56.49; H, 6.52; N, 9.30.

1-[2-(2,5-Dimethoxyphenyl)ethyl]-1-methylhydrazine Hydrogen Maleate (3j Hydrogen Maleate). Pinkish white crystalline substance, yield 1.60 g (49%); mp 84−87 °C (EtOH−Et_2O); ^{1}H NMR (400 MHz, D_2O) δ 3.02−3.09 (m, 5H, NCH_3, ArCH_2), 3.43−3.49 (m, 2H, NCH_2), 3.81 (s, 3H, OCH_3), 3.85 (s, 3H, OCH_3), 6.27 (s, 2H, CH=CH), 6.91−6.98 (m, 2H, C_6H_3), 7.04 (d, 1H, J = 8.9 Hz, C_6H_3). Anal. Calcd for $C_{15}H_{22}N_2O_6$: C, 55.21; H, 6.79; N, 8.58. Found: C, 55.03; H, 6.58; N, 8.41.

1-[2-(3,4-Dimethoxyphenyl)ethyl]-1-methylhydrazine Hydrochloride (3k Hydrochloride). White crystalline substance, yield 1.95 g (79%); mp 127−130 °C (MeOH−Et_2O); ^{1}H NMR (400 MHz, D_2O) δ 3.02−3.08 (m, 5H, ArCH_2, NCH_3), 3.46−3.52 (m, 2H, NCH_2), 3.86 (s, 3H, OCH$_3$), 3.88 (s, 3H, OCH$_3$), 6.92−6.97 (m, 1H, C_6H_3), 6.99−7.07 (m, 2H, C_6H_3).

Anal. Calcd for $C_{11}H_{19}ClN_2O_2$: C, 53.55; H, 7.76; N, 11.35. Found: C, 53.31; H, 7.87; N, 11.18.

1-[2-(2,3,4-Trimethoxyphenyl)ethyl]-1-methylhydrazine Hydrochloride (3l Hydrochloride). White crystalline solid, yield 1.80 g (65%); mp 129−131 °C (EtOH−Et_2O); ^{1}H NMR (400 MHz, D_2O) δ 3.01−3.09 (m, 5H, ArCH_2, NCH_3), 3.39−3.46 (m, 2H, NCH_2), 3.89 (s, 6H, 2 × OCH_3), 3.93 (s, 3H, OCH_3), 6.91 (d, 1H, J = 8.6 Hz, C_6H_2), 7.08 (d, 1H, J = 8.6 Hz, C_6H_2). Anal. Calcd for $C_{12}H_{21}ClN_2O_3$: C, 52.08; H, 7.65; N, 10.12. Found: C, 51.87; H, 7.42; N, 9.94.

1-[2-(3,4,5-Trimethoxyphenyl)ethyl]-1-methylhydrazine Hydrogen Maleate (3m Hydrogen Maleate). White crystalline solid, yield 2.56 g (72%); mp 76−78 °C (EtOH−Et_2O); ^{1}H NMR (400 MHz, D_2O) δ 3.01−3.12 (m, 5H, ArCH_2, NCH_3), 3.46−3.55 (m, 2H, NCH_2), 3.77 (s, 3H, OCH_3), 3.88 (s, 6H, 2 × OCH_3), 6.27 (s, 2H, CH=CH), 6.69 (s, 2H, C_6H_2). Anal. Calcd for $C_{16}H_{24}N_2O_7$: C, 53.92; H, 6.79; N, 7.86. Found: C, 53.99; H, 7.86; N, 7.73.

1-Ethyl-1-(2-phenylethyl)hydrazine Hydrogen Maleate (3n Hydrogen Maleate). White crystalline solid, yield 1.70 g (61%); mp 75−77 °C (EtOH−Et_2O); ^{1}H NMR (400 MHz, D_2O) δ 1.33 (t, 3H, J = 7.3 Hz, CH_3), 3.08−3.16 (m, 2H, ArCH_2), 3.37 (q, 2H, J = 7.3 Hz, CH_2CH$_3$), 3.47−3.57 (m, 2H, NCH_2), 6.29 (s, 2H, CH=CH), 7.32−7.45 (m, 5H, C_6H_5). Anal. Calcd for $C_{14}H_{20}N_2O_4$: C, 59.99; H, 7.19; N, 9.99. Found: C, 59.76; H, 6.93; N, 9.85.

1-Ethyl-1-[2-(4-methoxyphenyl)ethyl]hydrazine Hydrochloride (3o Hydrochloride). Yellowish white crystalline solid, yield 1.50 g (65%); mp 132−134 °C (MeOH−Et_2O); ^{1}H NMR (400 MHz, D_2O) δ 1.33 (t, 3H, J = 7.3 Hz, CH$_2$CH_3), 3.03−3.11 (m, 2H, ArCH_2), 3.35 (q, 2H, J = 7.3 Hz, CH_2CH$_3$), 3.43−3.51 (m, 2H, NCH_2), 3.84 (s, 3H, OCH_3), 7.02 (d, 2H, J = 8.8 Hz, C_6H_4), 7.31 (d, 2H, J = 8.8 Hz, C_6H_4). Anal. Calcd for $C_{11}H_{19}ClN_2O$: C, 57.26; H, 8.30; N, 12.14. Found: C, 57.49; H, 8.16; N, 11.96.

1-Ethyl-1-[2-(3,4,5-trimethoxyphenyl)ethyl]hydrazine Hydrochloride (3p Hydrochloride). White crystalline substance, yield 2.02 g (69%); mp 189−192 °C (MeOH−Et_2O); ^{1}H NMR (400 MHz, D_2O) δ 1.35 (t, 3H, J = 7.3 Hz, CH$_2$CH_3), 3.06−3.13 (m, 2H, ArCH_2), 3.37 (q, 2H, J = 7.3 Hz, CH_2CH$_3$), 3.48−3.56 (m, 2H, NCH_2), 3.79 (s, 3H, OCH_3), 3.89 (s, 6H, 2 × OCH_3), 6.73 (s, 2H, C_6H_2). Anal. Calcd for $C_{13}H_{23}ClN_2O_3$: C, 53.70; H, 7.97; N, 9.63. Found: C, 53.84; H, 8.08; N, 9.51.

1-Isobutyl-1-(2-phenylethyl)hydrazine Hydrogen Maleate (3q Hydrogen Maleate). White crystalline solid, yield 1.72 g (56%); mp 96−97 °C (EtOH−Et_2O); ^{1}H NMR (400 MHz, D_2O) δ 0.99 (d, 6H, J = 6.7 Hz, CH(CH_3)$_2$), 2.10−2.22 (m, 1H CH(CH$_3$)$_2$), 3.08−3.17 (m, 4H, ArCH_2, NCH_2), 3.45−3.54 (m, 2H, NCH_2), 6.29 (s, 2H, CH=CH), 7.31−7.45 (m, 5H, C_6H_5). Anal. Calcd for $C_{16}H_{24}N_2O_4$: C, 62.32; H, 7.84; N, 9.08. Found: C, 62.05; H, 7.58; N, 8.86.

1-Isobutyl-1-[2-(4-methoxyphenyl)ethyl]hydrazine Hydrogen Maleate (3r Hydrogen Maleate). Yellowish white crystalline solid, yield 2.15 g (64%); mp 109−111 °C (MeOH−Et_2O); ^{1}H NMR (400 MHz, D_2O) δ 0.99 (d, 6H, J = 6.6 Hz, CH(CH_3)$_2$), 2.09−2.22 (m, 1H CH(CH$_3$)$_2$), 3.02−3.16 (m, 4H, ArCH_2, NCH_2), 3.41−3.51 (m, 2H, NCH_2), 3.82 (s, 3H, OCH_3), 6.27 (s, 2H, CH=CH), 6.99 (d, 2H, J = 8.6 Hz, C_6H_4), 7.28 (d, 2H, J = 8.6 Hz, C_6H_4). Anal. Calcd for $C_{17}H_{26}N_2O_5$: C, 60.34; H, 7.74; N, 8.28. Found: C, 60.09; H, 7.63; N, 8.16.

1-Methyl-1-(3-phenylpropyl)hydrazine Hydrogen Maleate (3s Hydrogen Maleate). White crystalline solid, yield 2.10 g (75%); mp 71−72 °C (EtOH−Et_2O); ^{1}H NMR (400 MHz, D_2O) δ 2.03−2.14 (m, 2H, CH$_2$CH_2CH$_2$), 2.75 (t, 2H, J = 7.5 Hz, CH$_2$CH_2NCH$_3$), 3.02 (s, 3H, NCH_3), 3.23−3.29 (m, 2H, CH$_2$-CH_2C$_6$H$_4$), 6.31 (s, 2H, CH=CH), 7.29−7.45 (m, 5H, C_6H_5). Anal. Calcd for $C_{14}H_{20}N_2O_4$: C, 59.99; H, 7.19; N, 9.99. Found: C, 60.21; H, 7.35; N, 10.15.

2-(1-Methylhydrazino)-1-phenylethanol Hydrogen Maleate Hemiethanolate (9a Hydrogen Maleate Hemiethanolate). White crystalline substance, yield 1.52 g (54%); mp 63−66 °C (EtOH−Et_2O); ^{1}H NMR (400 MHz, D_2O) δ 3.06 (s, 3H, NCH_3), 3.40 (dd, 1H, J = 3.4, 13.3 Hz, NCH_2), 3.47 (dd, 1H, J = 9.9, 13.3 Hz, NCH_2), 5.18 (dd, 1H, J = 3.4, 9.9 Hz, OCH), 6.30 (s, 2H, CH=CH), 7.39−7.51 (m, 5H, C_6H_5). Anal. Calcd for $C_{13}H_{18}N_2O_5$: C, 55.31; H, 6.43; N, 9.92. Found: C, 55.26; H, 6.70; N, 9.87.

1-(2-Chlorophenyl)-2-(1-methylhydrazino)ethanol Hydrogen Fumarate (9b Hydrogen Fumarate). White crystalline solid, yield 2.06 g (65%); mp 127−128 °C (MeOH−Et_2O); ^{1}H NMR (400 MHz, D_2O) δ 3.07 (s, 3H, NCH_3), 3.32 (dd, 1H, J = 9.9, 13.4 Hz, NCH_2), 3.43 (dd, 1H, J = 2.8, 13.3 Hz, NCH_2), 5.56 (dd, 1H, J = 2.6, 9.8 Hz, OCH), 6.62 (s, 2H, CH=CH), 7.32−7.45 (m, 3H, C_6H_4), 7.59−7.63 (m, 1H, C_6H_4). Anal. Calcd for $C_{13}H_{17}ClN_2O_5$: C, 49.30; H, 5.41; N, 8.84. Found: C, 49.05; H, 5.15; N, 8.65.

1-(4-Chlorophenyl)-2-(1-methylhydrazino)ethanol (9c). White crystalline solid, yield 1.44 g (72%); mp 86−88 °C (Et_2O−*n*-hexane); ^{1}H NMR (400 MHz, $CDCl_3$) δ 2.48 (dd, 1H, J = 9.2, 12.8 Hz, NCH$_2$), 2.56 (s, 3H, NCH_3), 2.64 (dd, 1H, J = 2.3, 12.7 Hz, NCH$_2$), 4.98 (dd, 1H, J = 2.3, 9.3 Hz, OCH), 7.28−7.35 (m, 4H, C_6H_4). Anal. Calcd for $C_9H_{13}ClN_2O$: C, 53.87; H, 6.53; N, 13.96. Found: C, 53.59; H, 6.37; N, 13.75.

1-(3-Methoxyphenyl)-2-(1-methylhydrazino)ethanol Hydrogen Fumarate (9d Hydrogen Fumarate). White crystalline solid, yield 2.16 g (69%); mp 88−90 °C (EtOH−Et_2O); ^{1}H NMR (400 MHz, D_2O) δ 3.06 (s, 3H, NCH_3), 3.36 (dd, 1H, J = 9.9, 13.4 Hz, NCH$_2$), 3.47 (dd, 1H, J = 10.1, 13.3 Hz, NCH$_2$), 3.84 (s, 3H, OCH_3), 5.13 (dd, 1H, J = 3.2, 10.0 Hz, OCH), 6.66 (s, 2H, CH=CH), 7.03 (d, 2H, J = 8.4 Hz, C_6H_4), 7.41 (d, 2H, J = 8.8 Hz, C_6H_4). Anal. Calcd for $C_{14}H_{20}N_2O_6$: C, 53.84; H, 6.45; N, 8.97. Found: C, 53.57; H, 6.25; N, 8.73.

1-(4-Methoxyphenyl)-2-(1-methylhydrazino)ethanol Hydrogen Fumarate (9e Hydrogen Fumarate). White crystalline solid, yield 2.06 g (66%); mp 142−144 °C (EtOH−Et_2O); ^{1}H NMR (400 MHz, D_2O) δ 3.09 (s, 3H, NCH_3), 3.39 (dd, 1H, J = 3.4, 13.5 Hz, NCH$_2$), 3.50 (dd, 1H, J = 10.1, 13.4 Hz, NCH$_2$), 3.86 (s, 3H, OCH_3), 5.16 (dd, 1H, J = 3.3, 10.1 Hz, OCH), 6.68 (s, 2H, CH=CH), 7.06 (d, 2H, J = 8.8 Hz, C_6H_4), 7.41 (d, 2H, J = 8.8 Hz, C_6H_4). Anal. Calcd for $C_{14}H_{20}N_2O_6$: C, 53.84; H, 6.45; N, 8.97. Found: C, 53.59; H, 6.21; N, 8.70.

1-(4-Fluorophenyl)-2-(1-methylhydrazino)ethanol Hydrogen Maleate (9f Hydrogen Maleate). White crystalline solid, yield 1.89 g (63%); mp 101−104 °C (MeOH−Et_2O); ^{1}H NMR (400 MHz, D_2O) δ 3.05 (s, 3H, NCH_3), 3.36 (dd, 1H, J = 3.4, 13.4 Hz, NCH$_2$), 3.44 (dd, 1H, J = 10.1, 13.4 Hz, NCH$_2$), 5.16 (dd, 1H, J = 3.4, 9.9 Hz, OCH), 6.28 (s, 2H, CH=CH), 7.16 (dd, 2H, J = 8.8, 9.0 Hz, C_6H_4), 7.44 (dd, 2H, J = 5.5, 8.5 Hz, C_6H_4). Anal. Calcd for $C_{13}H_{17}FN_2O_5$: C, 52.00; H, 5.71; N, 9.33. Found: C, 52.24; H, 5.97; N, 9.58.

2-(1′-Methylhydrazino)-1-(2,3,4-trimethoxyphenyl)ethanol Hydrogen Fumarate (9g Hydrogen Fumarate). White crystalline solid, yield 2.42 g (65%); mp 139−141 °C (MeOH−Et_2O); ^{1}H NMR (500 MHz, D_2O) δ 3.06 (s, 3H, NCH_3), 3.26−3.45 (m, 2H, NCH$_2$), 3.86 (s, 3H, OCH_3), 3.88 (s, 3H, OCH_3), 3.92 (s, 3H, OCH_3), 5.36 (d, 1H, J = 8.4 Hz, OCH), 6.70 (s, 2H, CH=CH), 6.95 (d, 1H, J = 8.7 Hz, C_6H_2), 7.22 (d, 1H, J = 8.7, C_6H_2). Anal. Calcd for $C_{16}H_{24}N_2O_8$: C, 51.61; H, 6.50; N, 7.52. Found: C, 51.46; H, 6.43; N, 7.40.

1-(2,3-Dihydrobenzo[b][1,4]dioxin-6-yl)-2-(1-methylhydrazino)-ethanol Hydrogen Maleate (9h Hydrogen Maleate). White crystalline solid, yield 2.48 g (73%); mp 127−129 °C (MeOH−Et_2O); ^{1}H NMR (400 MHz, $CDCl_3$) δ 3.05 (s, 3H, NCH_3), 3.30−3.45 (m, 2H, NCH_2), 4.30 (s, 4H, OCH_2CH_2O), 5.07 (dd, 1H, J = 2.9, 9.8 Hz, OCH), 6.29 (s, 2H, CH=CH), 6.91−6.98 (m, 3H, C_6H_3). Anal. Calcd for $C_{15}H_{20}N_2O_7$: C, 52.94; H, 5.92; N, 8.23. Found: C, 52.66; H, 5.63; N, 8.00.

2-(1-Methylhydrazino)-1-(2-naphthyl)ethanol Hydrogen Maleate (9i Hydrogen Maleate). Yield 2.26 g (68%); mp 143−145 °C (MeOH−Et_2O); ^{1}H NMR (400 MHz, $CDCl_3$) δ 3.11 (s, 3H, NCH_3), 3.35−3.59 (m, 2H, NCH$_2$), 5.35 (dd, 1H, J = 2.9, 9.9 Hz, OCH), 6.19 (s, 2H, CH=CH), 7.53−7.62 (m, 3H, $C_{10}H_7$),

7.91−7.99 (m, 4H, $C_{10}H_7$). Anal. Calcd for $C_{17}H_{20}N_2O_5$: C, 61.44; H, 6.07; N, 8.43. Found: C, 61.71; H, 5.90; N, 8.23.

2-(1-Isobutylhydrazino)-1-phenylethanol Hydrogen Fumarate (9j Hydrogen Fumarate). White crystalline solid, yield 1.91 g (59%); mp 90−92 °C (EtOH−Et_2O); ^{1}H NMR (400 MHz, $CDCl_3$) δ 3.11 (d, 6H, J = 6.5 Hz, $CH(CH_3)_2$), 1.98−2.13 (m, 1H, $CH(CH_3)_2$), 2.98−3.92 (m, 2H, NCH_2), 3.30−3.48 (m, 2H, NCH_2) 5.24 (dd, 1H, J = 3.8, 9.1 Hz, OC*H*), 6.69 (s, 2H, C*H*=C*H*), 7.42−7.53 (m, 5H, C_6H_5). Anal. Calcd for $C_{16}H_{24}N_2O_5$: C, 59.24; H, 7.46; N, 8.64. Found: C, 59.32; H, 7.67; N, 8.85.

(1*R,2*S**)-2-(1-Methylhydrazino)-1-phenylpropan-1-ol Hydrochloride (10a Hydrochloride).** White crystalline solid, yield 1.63 g (75%); mp 145−146 °C (EtOH−Et_2O); ^{1}H NMR (400 MHz, D_2O) δ 1.22 (d, 3H, J = 7.0 Hz, $CHCH_3$), 2.99 (s, 3H, NCH_3), 3.66−3.73 (m, 1H, $CHCH_3$), 5.40−5.47 (m, 1H, C*H*OH), 7.41−7.54 (m, 5H, C_6H_5). Anal. Calcd for $C_{10}H_{17}ClN_2O$: C, 55.42; H, 7.91; N, 12.93. Found: C, 55.17; H, 7.65; N, 12.66.

(1*R,2*S**)-2-(1-Methylhydrazino)-1-phenylbutan-1-ol Hydrogen Fumarate (10b Hydrogen Fumarate).** White crystalline solid, yield 1.90 g (61%); mp 141−143 °C (EtOH−Et_2O); ^{1}H NMR (400 MHz, DMSO-d_6) δ 0.63 (t, 3H, J = 7.5 Hz, CH_2CH_3), 1.26−1.38 (m, 1H, CH_2), 1.49−1.62 (m, 1H, CH_2), 2.58−2.64 (m 4H, NCH_3, ArC*H*), 5.15 (d, 1H, J = 2.1 Hz, NC*H*), 6.55 (s, 2H, C*H*=C*H*), 7.17−7.38 (m, 5H, C_6H_5). Anal. Calcd for $C_{15}H_{22}N_2O_5$: C, 58.05; H, 7.15; N, 9.03. Found: C, 57.89; H, 7.02; N, 8.86.

(1*R,2*S**)-2-(1-Methylhydrazino)-1-phenylpentan-1-ol Hydrogen Fumarate (10c Hydrogen Fumarate).** White crystalline solid, yield 2.23 g (69%); mp 132−134 °C (EtOH−Et_2O); ^{1}H NMR (400 MHz, DMSO-d_6) 0.64 (t, 3H, J = 7.3 Hz, CH_2CH_3), 0.79−0.93 (m, 1H, CH_2), 1.07−1.31 (m, 2H, CH_2), 1.46−1.57 (m, 1H, CH_2), 2.60 (s, 3H, NCH_3), 2.66−2.71 (m, 1H, ArC*H*), 5.15 (d, 1H, J = 2.1 Hz, NC*H*), 6.57 (s, 2H, C*H*=C*H*), 7.16−7.37 (m, 5H, C_6H_5). Anal. Calcd for $C_{16}H_{24}N_2O_5$: C, 59.24; H, 7.46; N, 8.64. Found: C, 59.03; H, 7.28; N, 8.45.

2,2-Dimethyl-2-(1′-methylhydrazino)-1-phenylethanol Hydrogen Fumarate (10d Hydrogen Fumarate). White crystalline solid, yield 2.10 g (68%); mp 184−186 °C (MeOH−Et_2O); ^{1}H NMR (400 MHz, DMSO-d_6) 1.04 (s, 6H, 2 × CCH_3), 2.20 (s, 3H, NCH_3), 6.59 (s, 2H, C*H*=C*H*), 7.22−7.43 (m, 5H, C_6H_5). Anal. Calcd for $C_{15}H_{22}N_2O_5$: C, 58.05; H, 7.15; N, 9.03. Found: C, 57.92; H, 6.94; N, 8.95.

1-Benzyl-1-methylhydrazine Hydrogen Maleate (13 Hydrogen Maleate). White crystalline solid, yield 1.18 g (47%); mp 88−90 °C (MeOH−Et_2O); ^{1}H NMR (400 MHz, D_2O) δ 2.99 (s, 3H, CH_3), 4.38 (s, 2H, CH_2), 6.29 (s, 2H, CH=CH), 7.46−7.58 (m, 5H, C_6H_5). Anal. Calcd for $C_{12}H_{16}N_2O_4$: C, 57.13; H, 6.39; N, 11.10. Found: C, 57.01; H, 6.20; N, 10.98.

1-Methyl-1-(2-Phenylpropyl)hydrazine Hydrogen Fumarate (14b Hydrogen Fumarate). White crystalline solid, yield 1.88 g (67%); mp 143−146 °C (MeOH−Et_2O); ^{1}H NMR (400 MHz, D_2O) δ 1.31 (d, 3H, J = 7.0 Hz, CCH_3), 2,96 (s, 3H, NCH_3), 3.25−3.37 (m, 1H, C*H*), 3.44 (dd, 1H, J = 12.9, 5.9 Hz, CH_2), 3.55 (dd, 1H, J = 12.9, 9.9 Hz, CH_2), 6.67 (s, 2H, C*H*=C*H*), 7.34−7.49 (m, 5H, C_6H_5). Anal. Calcd for $C_{14}H_{20}N_2O_4$: C, 59.99; H, 7.19; N, 9.99. Found: C, 60.14; H, 7,01; N, 9.82.

2-(4-Methoxyphenyl)-1-(1′-methylhydrazino)-2-propanol Hydrogen Maleate (15 Hydrogen Maleate). White crystalline solid, yield 2.02 g (62%); mp 127−129 °C (MeOH−Et_2O); ^{1}H NMR (400 MHz, D_2O) δ 1.62 (s, 3H, CCH_3), 2.77 (s, 3H, NCH_3), 3.26−3.48 (m, 2H, CH_2), 3.84 (s, 3H, OCH_3), 6.30 (s, 2H, C*H*=C*H*), 7.05 (d, 2H, J = 8.8 Hz, C_6H_4), 7.47 (d, 2H, J = 8.8 Hz, C_6H_4). Anal. Calcd for $C_{15}H_{22}N_2O_6$: C, 55.21; H, 6.79; N, 8.58. Found: C, 55.03; H, 6.68; N, 8.50.

General Procedure for the Preparation of Hydrazino Alcohols 5a−c and 6a. To a stirred solution of hydrazine hydrate (12.5 g, 0.25 mol) in EtOH (10 mL), the corresponding styrene oxide (**4a−c**, 25 mmol) was added dropwise. The exothermic reaction brought the mixture to reflux. After addition was complete, the mixture was kept at 60 °C for 10 min. The solvent was evaporated off and the oily residue was dissolved in EtOH and treated with an equivalent amount of maleic acid. The separated crystals of the corresponding **5a−c** maleate were filtered off and recrystallized from EtOH. In case of compounds **a**, the filtrate was treated with Et_2O to give crystalline **6a** maleate which was filtered off and recrystallized twice from a mixture of EtOH and Et_2O.

2-Hydrazino-1-phenylethanol Hydrogen Maleate (5a Hydrogen Maleate). Beige crystalline solid, yield 3.22 g (48%); mp 120−122 °C (EtOH−Et_2O); ^{1}H NMR (D_2O) δ 3.38 (d, 2H, J = 7.9 Hz, NCH_2), 5.07 (t, 1H, J = 7.0 Hz, OC*H*), 6.29 (s, 2H, C*H*=C*H*), 7.39−7.52 (m, 5H, C_6H_5). Anal. Calcd for $C_{12}H_{16}N_2O_5$: C, 53.73; H, 6.01; N, 10.44. Found: C, 53.50; H, 5.83; N, 10.28.

2-Hydrazino-1-(3-methoxyphenyl)ethanol Hydrogen Maleate (5b Hydrogen Maleate). Pale yellow crystalline solid, yield 3.80 g (51%); mp 130−133 °C (EtOAc−MeOH); ^{1}H NMR (D_2O) δ 3.38 (d, 2H, J = 6.5 Hz, NCH_2), 3.87 (s, 3H, OCH_3), 5.07 (t, 1H, J = 6.5 Hz, OC*H*), 6.29 (s, 2H, C*H*=C*H*), 6.99−7.10 (m, 3H, C_6H_4), 7.42 (t, 1H, J = 7.9 Hz, C_6H_4). Anal. Calcd for $C_{13}H_{18}N_2O_6$: C, 52.34; H, 6.08; N, 9.39. Found: C, 52.52; H, 6.21; N, 9.65.

2-Hydrazino-1-(4-methoxyphenyl)ethanol Hydrogen Maleate (5c Hydrogen Maleate). Pale yellow crystalline solid, yield 3.51 g (47%); mp 117−120 °C (EtOH−Et_2O); ^{1}H NMR (D_2O) δ 3.32−3.45 (m, 2H, NCH_2), 3.87 (s, 3H, OCH_3), 5.04 (dd, 1H, J = 4.4, 8.8 Hz, OC*H*), 6.32 (s, 2H, C*H*=C*H*), δ 7.06 (d, 2H, J = 8.8 Hz, C_6H_4), 7.41 (d, 1H, J = 8.8 Hz, C_6H_4). Anal. Calcd for $C_{13}H_{18}N_2O_6$: C, 52.34; H, 6.08; N, 9.39. Found: C, 52.50; H, 6.17; N, 9.69.

2-Hydrazino-2-phenylethanol Hydrogen Maleate (6a Hydrogen Maleate). White crystalline solid, yield 0.80 g (12%); mp 107−110 °C (EtOH−Et_2O); ^{1}H NMR (D_2O) δ 3.91 (2H, m, OCH_2), 4.32 (1H, m, NC*H*), 6.31 (2H, s, C*H*=C*H*), 7.47 (5H, m, C_6H_5). Anal. Calcd for $C_{12}H_{16}N_2O_5$: C, 53.73; H, 6.01; N, 10.44. Found: C, 53.48; H, 5.78; N, 10.57.

General Procedure for the Preparation Hydrazino Alcohol O-Methyl Ethers 12a−j and O-Benzyl Ether 16. 55% Sodium hydride suspension (1.40 g, 32 mmol) was washed with *n*-hexane and suspended in THF (35 mL). A solution of the corresponding *N*-nitroso amino alcohol (**8**, 10 mmol) in THF (60 mL) was degassed with N_2 flushing and added dropwise to the NaH suspension with stirring and continuous N_2 flushing at 0 °C over a period of 1 h. Stirring was continued at 0 °C for 2 h, and then a solution of MeI (2.41 g, 17 mmol) or benzyl bromide (2.05 g, 12 mmol) in THF (20 mL) was added dropwise to the stirred suspension at 0 °C. The mixture was stirred at 0 °C for 30 min and then was allowed to warm to room temperature. The excess of NaH was decomposed by addition of MeOH. The solution evaporated to dryness, and the residue was dissolved in H_2O (40 mL) and extracted with EtOAc (3 × 40 mL). The combined EtOAc extracts were washed with H_2O (40 mL) and then dried (Na_2SO_4) and evaporated under reduced pressure to give the *O*-methyl-substituted product (**11a−j**) as a yellow oil.

The crude *O*-methyl-*N*-nitroso amino alcohol (**11a−j**) was dissolved in THF (20 mL) and was added dropwise to a strirred and ice-cooled suspension of $LiAlH_4$ (1.26 g, 33.2 mmol) in THF (60 mL). The mixture was stirred at 0 °C for 3 h, and then allowed to warm to room temperature. The excess of $LiAlH_4$ was decomposed with a mixture of H_2O (2.5 mL) and THF (20 mL), and the resulting precipitate was filtered off and washed with EtOAc (2 × 75 mL). The combined filtrates were dried (Na_2SO_4) and evaporated under reduced pressure. The oily residue was treated with an equivalent amount of maleic or fumaric acid in a mixture of EtOH and Et_2O to give crystalline hydrogen maleate or hydrogen fumarate salt which was filtered off and recrystallized.

1-[2-(3-Fluorophenyl)-2-methoxyethyl]-1-methylhydrazine Hydrogen Fumarate (12a Hydrogen Fumarate). White crystalline

solid, yield 1.67 g (53%); mp 108−110 °C (EtOH−Et_2O); ^{1}H NMR (400 MHz, D_2O) δ 3.21 (s, 3H, NCH_3), 3.47 (s, 3H, OCH_3), 3.52 (dd, 1H, J = 3.4, 13.8 Hz, NCH_2), 3.43 (dd, 1H, J = 10.1, 13.7 Hz, NCH_2), 4.96 (dd, 1H, J = 3.2, 10.3 Hz, OCH), 6.84 (s, 2H, CH=CH), 7.30−7.45 (m, 3H, C_6H_4), 7.61−7.69 (m, 1H, C_6H_4). Anal. Calcd for $C_{14}H_{19}FN_2O_5$: C, 53.50; H, 6.09; N, 8.91. Found: C, 53.24; H, 5.95; N, 8.70.

1-[2-(4-Fluorophenyl)-2-methoxyethyl]-1-methylhydrazine Hydrogen Fumarate (12b Hydrogen Fumarate). White crystalline solid, yield 1.70 g (54%); mp 117−119 °C (EtOH−Et_2O); ^{1}H NMR (500 MHz, D_2O) δ 3.02 (s, 3H, NCH_3), 3.24 (s, 3H, OCH_3), 3.30 (d, 1H, J = 13.8 Hz, NCH_2), 3.44 (dd, 1H, J = 10.1, 13.4 Hz, NCH_2), 4.75 (d, 1H, J = 9.8 Hz, OCH), 6.65 (s, 2H, CH=CH), 7.18 (dd, 2H, J = 7.4, 9.0 Hz C_6H_4), 7.41 (dd, 2H, J = 5.8, 7.8 Hz, C_6H_4). Anal. Calcd for $C_{14}H_{19}FN_2O_5$: C, 53.50; H, 6.09; N, 8.91. Found: C, 53.27; H, 5.91; N, 8.75.

1-(2-(3-Chlorophenyl)-2-methoxyethyl)-1-methylhydrazine Hydrogen Fumarate (12c Hydrogen Fumarate). White crystalline solid, yield 1.62 g (49%); mp 116−118 °C (EtOH−Et_2O); ^{1}H NMR (400 MHz, D_2O) δ 3.21 (s, 3H, NCH_3), 3.47 (s, 3H, OCH_3), 3.51 (dd, 1H, J = 3.1, 14.1 Hz, NCH_2), 3.63 (dd, 1H, J = 10.1, 13.7 Hz, NCH_2), 4.95 (dd, 1H, J = 3.1, 10.1 Hz, OCH), 6.85 (s, 2H, CH=CH), 7.51−7.55 (m, 1H, C_6H_4), 7.62−7.67 (m, 3H, C_6H_4). Anal. Calcd for $C_{14}H_{19}ClN_2O_5$: C, 50.84; H, 5.79; N, 8.47. Found: C, 51.00; H, 5.99; N, 8.70.

1-[2-(4-Chlorophenyl)-2-methoxyethyl]-1-methylhydrazine Hydrogen Maleate (12d Hydrogen Maleate). Yield 1.95 g (59%); mp 98−100 °C (EtOH−Et_2O); ^{1}H NMR (500 MHz, D_2O) δ 2.98 (s, 3H, NCH_3), 3.20−3.30 (m, 5H, OCH_3, NCH_2), 3.35−3.43 (m, 1H, NCH_2), 4.72 (dd, 1H, J = 2.5, 10.1 Hz, OCH), 6.25 (s, 2H, CH=CH), 7.34 (d, 2H, J = 8.3 Hz, C_6H_4), 7.43 (d, 2H, J = 8.3 Hz, C_6H_4). Anal. Calcd for $C_{14}H_{19}ClN_2O_5$: C, 50.84; H, 5.79; N, 8.47. Found: C, 50.59; H, 5.55; N, 8.19.

1-[2-Methoxy-1-(3-tolyl)ethyl]-1-methylhydrazine Hydrogen Fumarate (12e Hydrogen Fumarate). White crystalline solid, yield 1.74 g (56%); mp 116−119 °C (EtOH−Et_2O); ^{1}H NMR (400 MHz, D_2O) δ 2.37 (s, 3H, (CH_3)C_6H_4), 3.05 (s, 3H, NCH_3), 3.28 (s, 3H, OCH_3), 3.32 (dd, 1H, J = 2.8,14.0 Hz, NCH_2), 3.45 (dd, 1H, J = 10.4, 13.4 Hz, NCH_2), 4.74 (dd, 1H, J = 3.0, 10.3 Hz, OCH), 6.67 (s, 2H, CH=CH), 7.21−7.32 (m, 3H, C_6H_4), 7.37−7.42 (m, 1H, C_6H_4). Anal. Calcd for $C_{15}H_{22}N_2O_5$: C, 58.05; H, 7.15; N, 9.03. Found: C, 57.77; H, 6.93; N, 8.77.

1-[2-Methoxy-2-(3-methoxyphenyl)ethyl]-1-methylhydrazine Hydrogen Fumarate (12f Hydrogen Fumarate). Yield 1.99 g (61%); mp 140−143 °C (MeOH−Et_2O); ^{1}H NMR (400 MHz, D_2O) δ 3.03 (s, 3H, NCH_3), 3.27 (s, 3H, OCH_3), 3.31 (dd, 1H, J = 3.5, 13.8 Hz, NCH_2), 3.45 (dd, 1H, J = 10.3, 13.6 Hz, NCH_2), 3.84 (s, 3H, (CH_3O)C_6H_4), 4.74 (dd, 1H, J = 3.2, 10.4 Hz, OCH), 6.65 (s, 2H, CH=CH), 6.99−7.05 (m, 3H, C_6H_4), 7.41 (t, 1H, J = 8.1 Hz, C_6H_4). Anal. Calcd for $C_{15}H_{22}N_2O_6$: C, 55.21; H, 6.80; N, 8.58. Found: C, 55.48; H, 7.05; N, 8.95.

1-[2-Methoxy-1-(4-methoxyphenyl)ethyl]-1-methylhydrazine Hydrogen Fumarate (12g Hydrogen Fumarate). Pale yellow crystalline solid, yield 1.96 g (60%); mp 104−107 °C (EtOH−Et_2O); ^{1}H NMR (400 MHz, D_2O) δ 3.07 (s, 3H, NCH_3), 3.27 (s, 3H, OCH_3), 3.33 (dd, 1H, J = 3.3, 13.8 Hz, NCH_2), 3.51 (dd, 1H, J = 10.7, 13.8 Hz, NCH_2), 3.87 (s, 3H, (CH_3O)C_6H_4), 4.74 (dd, 1H, J = 3.1, 10.5 Hz, OCH), 6.68 (s, 2H, CH=CH), 7.08 (d, 2H, J = 8.8 Hz, C_6H_4), 7.39 (d, 2H, J = 8.8 Hz, C_6H_4). Anal. Calcd for $C_{15}H_{22}N_2O_6$: C, 55.21; H, 6.80; N, 8.58. Found: C, 55.47; H, 7.01; N, 8.85.

1-[2-Methoxy-2-(2,3,4-trimethoxyphenyl)ethyl]-1-methylhydrazine Hydrogen Fumarate (12h Hydrogen Fumarate). Beige crystalline solid, yield 1.97 g (51%); mp 122−124 °C (MeOH−Et_2O); ^{1}H NMR (500 MHz, $CDCl_3$) δ 2.80 (s, 3H, NCH_3), 3.44 (s, 3H, OCH_3), 3.76−3.85 (m, 1H, NCH), 3.88 (s, 3H, OCH_3), 3.91 (s, 3H, OCH_3), 3.94 (s, 3H, OCH_3), 4.07−4.15 (m, 1H, NCH), 4.70−4.80 (br s, overlapped with the peak of the residual H_2O, 1H, OCH), 6.61 (s, 2H, CH=CH), 6.96 (d, 1H, J = 8.6 Hz, C_6H_2), 7.22 (d, 1H, J = 8.6 Hz, C_6H_2). Anal. Calcd for $C_{17}H_{26}N_2O_8$: C, 52.84; H, 6.78; N, 7.25. Found: C, 52.60; H, 6.63; N, 7.19.

1-[2-Methoxy-2-(1-naphthyl)ethyl]-1-methylhydrazine Hydrogen Fumarate (12i Hydrogen Fumarate). Yield 2.01 g (58%); mp 147−149 °C (MeOH−Et_2O); ^{1}H NMR (400 MHz, D_2O) δ 3.11 (s, 3H, NCH_3), 3.37 (s, 3H, OCH_3), 3.48 (dd, 1H, J = 3.0, 13.8 Hz, NCH_2), 3.63 (dd, 1H, J = 10.4, 13.8 Hz, NCH_2), 5.61 (dd, 1H, J = 3.4, 10.8 Hz, OCH), 6.67 (s, 2H, CH=CH), 7.60−7.72 (m, 4H, $C_{10}H_7$), 8.01 (d, 1H, J = 8.1 Hz, $C_{10}H_7$), 8.05 (d, 1H, J = 8.1 Hz, $C_{10}H_7$), 8.22 (d, 1H, J = 8.1 Hz, $C_{10}H_7$). Anal. Calcd for $C_{18}H_{22}N_2O_5$: C, 62.42; H, 6.40; N, 8.09. Found: C, 62.70; H, 6.67; N, 8.38.

1-[2-Methoxy-2-(2-naphthyl)ethyl]-1-methylhydrazine Hydrogen Maleate (12j Hydrogen Maleate). Yield 1.94 g (56%); mp 119−120 °C (MeOH−Et_2O); ^{1}H NMR (400 MHz, D_2O) δ 3.09 (s, 3H, NCH_3), 3.33 (s, 3H, OCH_3), 3.41 (dd, 1H, J = 2.8, 13.6 Hz, NCH_2), 3.63 (dd, 1H, J = 10.5, 13.6 Hz, NCH_2), 4.95 (dd, 1H, J = 2.6, 10.4 Hz, OCH), 6.25 (s, 2H, CH=CH), 7.54 (dd, 1H, J = 1.7, 8.8 Hz, $C_{10}H_7$), 7.60−7.65 (m, 2H, $C_{10}H_7$), 7.95−8.04 (m, 4H, $C_{10}H_7$). Anal. Calcd for $C_{18}H_{22}N_2O_5$: C, 62.42; H, 6.40; N, 8.09. Found: C, 62.17; H, 6.15; N, 8.38.

1-[2-Benzyloxy-2-(4-methoxyphenyl)ethyl]-1-methylhydrazine Hydrogen Fumarate (16 Hydrogen Fumarate). Beige crystalline solid, yield 1.52 g (38%); mp 118−120 °C (EtOH−Et_2O); ^{1}H NMR (400 MHz, D_2O) δ 2.97 (s, 3H, NCH_3), 3.31 (dd, 1H, J = 13.4, 3.0 Hz, NCH), 3.54 (dd, 1H, J = 13.4, 10.4 Hz, NCH), 3.86 (s, 3H, OCH_3), 4.37 (d, 1H, J = 11.3 Hz, OCH_2), 4.49 (d, 1H, J = 11.3 Hz, OCH_2), 4.87 (dd, 1H, J = 10.4, 3.0 Hz, OCH), 6.66 (s, 2H, CH=CH), 7.07 (d, 2H, J = 8.6 Hz, C_6H_4), 7.32−7.46 (m, 7H, C_6H_4, C_6H_5). Anal. Calcd for $C_{21}H_{26}N_2O_6$: C, 62.67; H, 6.51; N, 6.96. Found: C, 62.49; H, 6.71; N, 7.11.

1-(2-Phenylpropyl)hydrazine Hydrogen Fumarate (14a Hydrogen Fumarate). 2-Phenylpropyl bromide (1.99 g, 10 mmol) was added dropwise to a stirred refluxing solution of hydrazine hydrate (6.00 g, 0.12 mol) in EtOH (10 mL). The solution was refluxed for 22 h and evaporated in vacuo. Et_2O (25 mL) and K_2CO_3 (5 g) was added to the residue and the mixture was stirred for 15 min at ambient temperature. It was then filtered and evaporated. The oily residue was treated with an equivalent amount of fumaric acid in a mixture of EtOH and Et_2O to give a crystalline hydrogen fumarate salt. The crystalline product was filtered off and recrystallized.

White crystalline solid; yield 1.24 g (47%); mp 126−129 °C (EtOH−Et_2O); ^{1}H NMR (400 MHz, D_2O) δ 1.32 (d, 3H, J = 6.8 Hz, CH_3), 3.10−3.23 (m, 1H, CH), 3.30−3.42 (m, 2H, CH_2), 6.67 (s, 2H, CH=CH), 7.28−7.47 (m, 5H, C_6H_5). Anal. Calcd for $C_{13}H_{18}N_2O_4$: C, 58.63; H, 6.81; N, 10.52. Found: C, 58.75; H, 6.62; N, 10.37.

Expression of Recombinant VAP-1. Recombinant VAP-1 protein was obtained from Chinese hamster ovary (CHO) cells stably transfected with a full-length human VAP-1 cDNA. Recombinant human VAP-1 SSAO expressed in CHO cells was used as a source of VAP-1 SSAO for activity measurements. Native CHO cells have negligible SSAO activity. These cells and their culture have previously been described.[8] A cell lysate was prepared by suspending approximately 3.6 × 108 cells in 25 mL lysis buffer (150 mM NaCl, 10 mM Tris-Base pH 7.2, 1.5 mM $MgCl_2$, 1% NP40) and incubating at 4 °C overnight on a rotating table. The lysate was clarified by centrifugation at 18000g for 5 min at room temperature and the supernatant was used directly in the assay.

Mitochondrial MAO Extract. Rat total monoamine oxidase enzyme (MAO, mixture of MAO A and MAO B) was prepared from rat liver tissues by rinsing the liver sample several times in KCl-EDTA-solution to remove all blood. Then the liver sample was homogenized in ice-cold potassium phosphate buffer (0.1 M, pH 7.4) with an Ultra-Turax homogenizer (setting 11 000 rpm, 4 × 10 s). After centrifugation at 500g for 10 min at 4 °C the supernatant was carefully withdrawn and was centrifuged at 12300g for 15 min at 4 °C. The supernatant was

discharged and sedimented mitochondria were resuspended in fresh phosphate buffer and centrifuged as previously. The mitochondria were suspended in phosphate buffer and homogenized with an Ultra-Turax homogenizer (setting 11 000 rpm, 2×10 s). Mitochondrial preparate was aliquoted and stored at −70 °C.

In Vitro Inhibition of VAP-1 SSAO Activity. VAP-1 SSAO activity was measured using the coupled colorimetric method essentially as described for monoamine oxidase and related enzymes.[48] The VAP-1 SSAO assay was performed in 96 well microtiter plates as follows. To each well was added a predetermined amount of inhibitor if required. The amount of inhibitor varied in each assay but was generally at a final concentration of between 1 nM and 50 μM. Controls lacked inhibitor. The inhibitor was in a total volume of 20 μL in water. The assay was performed in a final volume of 200 μL consisting of 0.2 M potassium phosphate buffer (pH 7.6) and freshly made chromogenic solution containing 1 mM 2,4-dichlorophenol, 500 μM 4-aminoantipyrine and 4 U/mL horseradish peroxidase and an amount of CHO cell lysate containing VAP-1 SSAO that caused a change of 0.6 A_{490} per h. This was within the linear response range of the assay. The plates were incubated for 30 min at 37 °C and the background absorbance measured at 490 nm using a Wallac Victor II multilabel counter. To initiate the enzyme reaction 10 mM benzylamine (final concentration = 1 mM) was added and the plate incubated for 1 h at 37 °C. The increase in absorbance, reflecting VAP-1 SSAO activity, was measured at 490 nm. Inhibition was presented as percent inhibition compared to control after correcting for background absorbance and IC_{50} values calculated using GraphPad Prism.

Comparison of VAP-1 SSAO Activity versus Rat Total MAO Activity. Total MAO activity was measured in a similar way as for VAP-1 SSAO except that 2,4-dichlorophenol was replaced by 1 mM vanillic acid. To each well was added a predetermined amount of inhibitor if required. The amount of inhibitor varied in each assay but was generally at a final concentration of between 10 nM and 800 μM. Controls lacked inhibitor. The inhibitor was in a total volume of 20 μL in water. The assay was performed in a final volume of 300 μL consisting of 0.2 M potassium phosphate buffer (pH 7.6) and of freshly made chromogenic solution (as above) and total MAO preparation. The plates were incubated for 30 min at 37 °C and the background absorbance measured at 490 nm using a Wallac Victor II multilabel counter. To initiate the enzyme reaction 5 mM tyramine (final concentration 0.5 mM) was added and the plate incubated for 1 h at 37 °C. The increase in absorbance, reflecting total MAO activity, was measured at 490 nm. Inhibition was presented as percent inhibition compared to control after correcting for background absorbance and IC_{50} values calculated using GraphPad Prism. Clorgyline and pargyline (inhibitors of MAO A and MAO B, respectively) at 0.5 μM were added to some wells as positive controls for MAO inhibition.

Starting Structures for Molecular Dynamics Simulations. A 3D structure of VAP-1 with TPQ in an active conformation (PDB ID 2C11, resolution of 2.90 Å)[10] without a bound 2-hydrazinopyridine ligand was used in the MD simulations. All studied inhibitor molecules bind covalently to TPQ (called thereafter as TPQ-ligand complex) and they were parametrized as following: (1) TPQ-ligand complex was build with SYBYL 7.3,[49] (2) optimized with GAUSSIAN03[50] at the HF/6-31+G* level, (3) the electrostatic potentials of the ligand were calculated with GAUSSIAN03 (HF/6-31+G*) for the optimized TPQ-ligand complex, and (4) the RESP methodology[51] was used to create the atom-centered point charges from the electrostatic potentials. The charges of chemically comparable atoms in the ligand molecules were set to identical values.

To maintain the coordination of three histidines (HID520, HID522, and HIE684) to the Cu^{2+} ion, the negative charges of the coordinating N-atoms were increased in order to keep the Cu^{2+} ion in the coordination site throughout the MD simulation [(HID(520, 522)$^{N\delta}$: −0.76; HIE(684)$^{N\varepsilon}$ −0.93]. Finally, hydrogens, neutralizing counterions, and TIP3P water molecules extending 13 Å around the protein complex (rectangular box) were added with LEAP.[52]

Molecular Dynamics Simulations. All energy minimizations and molecular dynamics simulations were performed with NAMD 2.6[53] using ff03 force field parameters[54] for the protein and gaff99 parameters[55] for the ligands (TPQ + compound **5a**, Table 1). The whole MD simulation procedure comprised of two minimization runs and two MD simulation runs. (1) The water molecules, counterions, and amino acid side chains were minimized with the conjugate gradient algorithm (3000 steps) as rest of the complex was constrained by restraining Cα-atoms into their initial positions with the harmonic force of 5 kcal mol^{-1} Å^{-2}. (2) The whole system was minimized without constraints (3000 steps) to make sure complete equilibration; (3) the first MD simulation (360 ps), where the Cα-atoms were restrained as in step (1), was performed in the constant pressure, and (4) the 2.4 ns production simulation was performed without constraints. Since large conformation changes are not likely on inhibitor binding, the 2.4 ns were considered to be long enough simulation time.

The simulated complex was held at constant temperature (300 K) with Langevin dynamics for all non-hydrogen atoms, using a Langevin damping coefficient of 5 ps^{-1}. A constant pressure of 1 atm was upheld by a Nosé-Hoover Langevin piston[56] with an oscillation time scale of 200 fs and a damping time scale of 100 fs. An integration time step of 2 fs was used under a multiple time stepping scheme.[57] The bonded and short-range interactions were calculated every time step and long-range electrostatic interactions every third step. A cutoff value of 12 Å was used for the van der Waals and short-range electrostatic interactions. A switching function was enforced for the van der Waals forces to smoothen the cutoff. The simulations were conducted under the periodic boundary conditions with the full-system, and the long-range electrostatics were counted with the particle-mesh Ewald method.[58] The bonds involving hydrogen atoms were restrained by the SHAKE algorithm.[59]

Starting Structures for 3D QSAR. The crystal structure of VAP-1 in complex with 2-hydrazinopyridine[10] was retrieved from the Protein Data Bank.[60] The conformation of the side chain of Leu469 was changed to resemble that obtained from MD simulations (see Results and Discussion) using amino acid side-chain rotamer library[61] incorporated into BODIL modeling environment.[62] In addition, the water molecules and the atoms of bound inhibitor molecule 2-hydrazinopyridine (C1, C2, C3, C4, C5, and N3 in the crystal structure) were removed. Hydrogen atoms were added using SYBYL.[49]

Construction of Ligands for 3D QSAR. Ligands were sketched in SYBYL[49] and energy was minimized by using MMFF94s[63] force field with MMFF94 charges and conjugate gradient method until the energy gradient was less than 0.05 kcal/mol. All possible enantiomers were built.

Docking Simulations. Bioactive conformations for studied ligands were predicted with GOLD 3.1.1.[64,65] The ligand binding pocket was defined using the $C^{\beta}H$ from Leu468 as a central atom with radius of 20 Å. The ligands were docked covalently to nitrogen atom N1 of PAQ1729 (PAQ is used in PDB file (PDB-code: 2C11[10]) to assign TPQ and the 2-hydrazinopyridine covalently bonded to it). Each ligand was docked 10 times; however, the docking simulation was allowed to terminate in cases where the root-mean-squared deviations (rmsd) of three best conformations were within 1.5 Å.

3D QSAR Analysis. The superpositioning of ligands for 3D QSAR was obtained by using the first ranked conformation for each ligand from docking by using the fitness function of GOLD. The CoMSIA method in SYBYL[49] was used for model building to explore physicochemical properties that contribute to the correlation. The CoMSIA descriptors for steric and hydrophobic fields were calculated in SYBYL[49] using default

settings, and were used for model building. The correlation of these fields with the $-\log IC_{50}$ values was calculated by using the partial least-squares (PLS) method.[66] Column filtering of 0.5 kcal/mol was used for leave-one-out (LOO) cross-validations. The built models were validated as follows: (1) the 47 molecules were sorted according to their experimental data, (2) molecules were divided into four sets that where equal in size (one containing 11 and three containing 12 molecules) and diversity in VAP-1 potency, (3) three out of four sets were used to build a QSAR model, and the potencies for the molecules in the fourth set were predicted. Finally, all 47 molecules were used to build a 3D QSAR model for both VAP-1 and MAO. Thus, in total, 10 QSAR models were made: five for VAP-1 (one that contained all 47 molecules and four containing 3/4 of molecules), and similarly five for MAO.

The validation of the VAP-1 and MAO models was done using progressive scrambling[45] and bootstrapping.[46,47] In progressive scrambling the maximum number of bins was set to 10 and the minimum number of bins was set to 2. The default value of 0.85 was used for critical point, and a total of 100 scramblings were used for both VAP-1 and MAO models. Progressive scrambling was performed five times for both models and average values were calculated for parameters. The parameters acquired from the progressive scrambling are (1) q^{**2} which indicates the predictivity of the model after potential effects of redundancy have been removed, that is, the expected value of q^2 at the specified critical point, (2) cSDEP which is the estimated crossvalidated standard error at the specified critical point for $r^2_{yy'}$ (the correlation of the scrambled responses with the unperturbed data), and (3) $dq^{2'}/dr^2_{yy}$ which is the slope of q^2 (the crossvalidated correlation coefficient) evaluated at the specified critical point with respect to the correlation of the original dependent variables versus the perturbed dependent variables. The value of the slope should be under 1 as the values over 1 indicate the overfitting of the model. For bootstrapping validation 100 runs were performed.

Acknowledgment. This study was supported by the Sigrid Jusélius Foundation (OTP), Academy of Finland (UP Grant Number 121393), and CSC-Finnish IT Center for Science (OTP: jyy2516).

Supporting Information Available: Table S1: The melting points of synthesized hydrazine molecules and the number of the submodel where a compound belongs in QSAR model building. Table S2: Statistics of different COMSIA 3D QSAR models. Figure S1: Visualization of additional COMSIA-models. This information is available free of charge via the Internet at http://pubs.acs.org/.

References

(1) Yu, P. H.; Lu, L. X.; Fan, H.; Kazachkov, M.; Jiang, Z. J.; Jalkanen, S.; Stolen, C. Involvement of semicarbazide-sensitive amine oxidase-mediated deamination in lipopolysaccharide-induced pulmonary inflammation. *Am. J. Pathol.* **2006**, *168*, 718–726.

(2) Yu, P. H.; Deng, Y. L. Endogenous formaldehyde as a potential factor of vulnerability of atherosclerosis: involvement of semicarbazide-sensitive amine oxidase-mediated methylamine turnover. *Atherosclerosis* **1998**, *140*, 357–363.

(3) Janes, S. M.; Mu, D.; Wemmer, D.; Smith, A. J.; Kaur, S.; Maltby, D.; Burlingame, A. L.; Klinman, J. P. A new redox cofactor in eukaryotic enzymes: 6-hydroxydopa at the active site of bovine serum amine oxidase. *Science* **1990**, *248*, 981–987.

(4) Wang, S. X.; Mure, M.; Medzihradszky, K. F.; Burlingame, A. L.; Brown, D. E.; Dooley, D. M.; Smith, A. J.; Kagan, H. M.; Klinman, J. P. A crosslinked cofactor in lysyl oxidase: redox function for amino acid side chains. *Science* **1996**, *273*, 1078–1084.

(5) Carpene, C.; Visentin, V.; Morin, N.; Prevot, D.; Smih, F.; Rouet, P.; Jayat, D.; Fontana, E.; Lizcano, J. M. Characterization of semicarbazide-sensitive amine oxidase in human subcutaneous adipocytes and search for novel functions. *Inflammopharmacology* **2003**, *11*, 119–126.

(6) Houslay, M. D.; Tipton, K. F. A kinetic evaluation of monoamine oxidase activity in rat liver mitochondrial outer membranes. *Biochem. J.* **1974**, *139*, 645–652.

(7) Ochiai, Y.; Itoh, K.; Sakurai, E.; Adachi, M.; Tanaka, Y. Substrate selectivity of monoamine oxidase A, monoamine oxidase B, diamine oxidase, and semicarbazide-sensitive amine oxidase in COS-1 expression systems. *Biol. Pharm. Bull.* **2006**, *29*, 2362–2366.

(8) Smith, D. J.; Salmi, M.; Bono, P.; Hellman, J.; Leu, T.; Jalkanen, S. Cloning of vascular adhesion protein 1 reveals a novel multifunctional adhesion molecule. *J. Exp. Med.* **1998**, *188*, 17–27.

(9) Jalkanen, S.; Salmi, M. Cell surface monoamine oxidases: enzymes in search of a function. *EMBO J.* **2001**, *20*, 3893–3901.

(10) Jakobsson, E.; Nilsson, J.; Ogg, D.; Kleywegt, G. J. Structure of human semicarbazide-sensitive amine oxidase/vascular adhesion protein-1. *Acta Crystallogr. D Biol. Crystallogr.* **2005**, *61*, 1550–1562.

(11) Airenne, T. T.; Nymalm, Y.; Kidron, H.; Smith, D. J.; Pihlavisto, M.; Salmi, M.; Jalkanen, S.; Johnson, M. S.; Salminen, T. A. Crystal structure of the human vascular adhesion protein-1: unique structural features with functional implications. *Protein Sci.* **2005**, *14*, 1964–1974.

(12) Marttila-Ichihara, F.; Smith, D. J.; Stolen, C.; Yegutkin, G. G.; Elima, K.; Mercier, N.; Kiviranta, R.; Pihlavisto, M.; Alaranta, S.; Pentikäinen, U.; Pentikäinen, O.; Fülöp, F.; Jalkanen, S.; Salmi, M. Vascular amine oxidases are needed for leukocyte extravasation into inflamed joints in vivo. *Arthritis Rheum.* **2006**, *54*, 2852–2862.

(13) Akin, E.; Aversa, J.; Steere, A. C. Expression of adhesion molecules in synovia of patients with treatment-resistant lyme arthritis. *Infect. Immun.* **2001**, *69*, 1774–1780.

(14) Boomsma, F.; Derkx, F. H.; van den Meiracker, A. H.; Man in 't Veld, A. J.; Schalekamp, M. A. Plasma semicarbazide-sensitive amine oxidase activity is elevated in diabetes mellitus and correlates with glycosylated haemoglobin. *Clin. Sci.* (*London*) **1995**, *88*, 675–679.

(15) Boomsma, F.; Bhaggoe, U. M.; van der Houwen, A. M.; van den Meiracker, A. H. Plasma semicarbazide-sensitive amine oxidase in human (patho)physiology. *Biochim. Biophys. Acta* **2003**, *1647*, 48–54.

(16) Garpenstrand, H.; Ekblom, J.; Backlund, L. B.; Oreland, L.; Rosenqvist, U. Elevated plasma semicarbazide-sensitive amine oxidase (SSAO) activity in Type 2 diabetes mellitus complicated by retinopathy. *Diabet. Med.* **1999**, *16*, 514–521.

(17) Weiss, H. G.; Klocker, J.; Labeck, B.; Nehoda, H.; Aigner, F.; Klingler, A.; Ebenbichler, C.; Foger, B.; Lechleitner, M.; Patsch, J. R.; Schwelberger, H. G. Plasma amine oxidase: a postulated cardiovascular risk factor in nondiabetic obese patients. *Metabolism* **2003**, *52*, 688–692.

(18) Boomsma, F.; van Veldhuisen, D. J.; de Kam, P. J.; Man in't Veld, A. J.; Mosterd, A.; Lie, K. I.; Schalekamp, M. A. Plasma semicarbazide-sensitive amine oxidase is elevated in patients with congestive heart failure. *Cardiovasc. Res.* **1997**, *33*, 387–391.

(19) Mathys, K. C.; Ponnampalam, S. N.; Padival, S.; Nagaraj, R. H. Semicarbazide-sensitive amine oxidase in aortic smooth muscle cells mediates synthesis of a methylglyoxal-AGE: implications for vascular complications in diabetes. *Biochem. Biophys. Res. Commun.* **2002**, *297*, 863–869.

(20) Wang, E. Y.; Gao, H.; Salter-Cid, L.; Zhang, J.; Huang, L.; Podar, E. M.; Miller, A.; Zhao, J.; O'rourke, A.; Linnik, M. D. Design, synthesis, and biological evaluation of semicarbazide-sensitive amine oxidase (SSAO) inhibitors with anti-inflammatory activity. *J. Med. Chem.* **2006**, *49*, 2166–2173.

(21) Yabanoglu, S.; Ucar, G.; Gokhan, N.; Salgin, U.; Yesilada, A.; Bilgin, A. A. Interaction of rat lung SSAO with the novel 1-N-substituted thiocarbamoyl-3-substituted phenyl-5-(2-pyrolyl)-2-pyrazoline derivatives. *J. Neural Transm.* **2007**, *114*, 769–773.

(22) Olarte, A. Z.; Mian, A.; Clauzel, L. M.; Exposito, M. R.; Font, F. Y.; Palomera, F. A. WO 2006013209, 2006.

(23) Clauzel, L. M.; Font, F. Y.; Vicente, S. G.; Exposito, M. R.; Palomera, F. A.; Olarte, A. Z. US 2007066646 A1 20070322, 2007.

(24) Olivieri, A.; Tipton, K.; O'Sullivan, J. L-Lysine as a recognition molecule for the VAP-1 function of SSAO. *J. Neural Transm.* **2007**, *114*, 747–749.

(25) Yegutkin, G. G.; Salminen, T.; Koskinen, K.; Kurtis, C.; McPherson, M. J.; Jalkanen, S.; Salmi, M. A peptide inhibitor of vascular adhesion protein-1 (VAP-1) blocks leukocyte-endothelium interactions under shear stress. *Eur. J. Immunol.* **2004**, *34*, 2276–2285.

(26) Wang, X.; Pietrangeli, P.; Mateescu, M. A.; Mondovi, B. Extended substrate specificity of serum amine oxidase: possible involvement in protein posttranslational modification. *Biochem. Biophys. Res. Commun.* **1996**, *223*, 91–97.

(27) Kirton, C. M.; Laukkanen, M. L.; Nieminen, A.; Merinen, M.; Stolen, C. M.; Armour, K.; Smith, D. J.; Salmi, M.; Jalkanen, S.; Clark, M. R. Function-blocking antibodies to human vascular adhesion protein-1: a potential anti-inflammatory therapy. *Eur. J. Immunol.* **2005**, *35*, 3119–3130.
(28) Jalkanen, S.; Jalkanen, M.; Salmi, M. WO/2006/134203, 2006.
(29) De Colibus, L.; Li, M.; Binda, C.; Lustig, A.; Edmondson, D. E.; Mattevi, A. Three-dimensional structure of human monoamine oxidase A (MAO A): relation to the structures of rat MAO A and human MAO B. *Proc. Natl. Acad. Sci. U. S. A.* **2005**, *102*, 12684–12689.
(30) Son, S. Y.; Ma, J.; Kondou, Y.; Yoshimura, M.; Yamashita, E.; Tsukihara, T. Structure of human monoamine oxidase A at 2.2-Å resolution: the control of opening the entry for substrates/inhibitors. *Proc. Natl. Acad. Sci. U. S. A.* **2008**, *105*, 5739–5744.
(31) Binda, C.; Hubalek, F.; Li, M.; Herzig, Y.; Sterling, J.; Edmondson, D. E.; Mattevi, A. Crystal structures of monoamine oxidase B in complex with four inhibitors of the N-propargylaminoindan class. *J. Med. Chem.* **2004**, *47*, 1767–1774.
(32) Binda, C.; Newton-Vinson, P.; Hubalek, F.; Edmondson, D. E.; Mattevi, A. Structure of human monoamine oxidase B, a drug target for the treatment of neurological disorders. *Nat. Struct. Biol.* **2002**, *9*, 22–26.
(33) Binda, C.; Wang, J.; Pisani, L.; Caccia, C.; Carotti, A.; Salvati, P.; Edmondson, D. E.; Mattevi, A. Structures of human monoamine oxidase B complexes with selective noncovalent inhibitors: safinamide and coumarin analogs. *J. Med. Chem.* **2007**, *50*, 5848–5852.
(34) Binda, C.; Wang, J.; Li, M.; Hubalek, F.; Mattevi, A.; Edmondson, D. E. Structural and mechanistic studies of arylalkylhydrazine inhibition of human monoamine oxidases A and B. *Biochemistry* **2008**, *47*, 5616–5625.
(35) Ragnarsson, U. Synthetic methodology for alkyl substituted hydrazines. *Chem. Soc. Rev.* **2001**, *30*, 205–213.
(36) Zalan, Z.; Lazar, L.; Fülöp, F. Chemistry of hydrazinoalcohols and their heterocyclic derivatives. Part 1. Synthesis of hydrazinoalcohols. *Curr. Org. Chem* **2005**, *9*, 357–376.
(37) Kim, M.; White, J. D. Olefins from thermal decomposition of N-sulfoximino-2-oxazolidones. A novel synthesis of bicyclo-[3.3.1]non-1-ene. *J. Am. Chem. Soc.* **1977**, *99*, 1172–1180.
(38) Roth, H. J.; Brandau, A. On the aminolysis of styroloxide, preparation of phenylaminoethanols. Part IV. Aminolysis of epoxide. *Arch. Pharm.* **1959**, *292/64*, 761–777.
(39) Coote, S. J.; Davies, S. G.; Middlemiss, D.; Naylor, A. Enantiospecific synthesis of (+)-(*R*)-6,7-dimethoxy-2-methyl-4-phenyl-1,2,3,4-tetrahydroisoquinoline from (+)-(*S*)-2-methylamino-1-phenylethanol. *J. Chem. Soc., Perkin Trans. 1* **1989**, 2223−2228.
(40) Rosenmund, K. W.; Karg, E.; Marcus, F. K. Preparation of beta-arylalkylamines. *Chem. Ber.* **1942**, 1850–1859.
(41) Schulz, H. Preparation of cardiac- and circulatory-active compounds. *Pharmazie* **1967**, *22*, 19–22.
(42) Lövgren, K.; Nilsson, J. L. Adrenergic receptor agonists. Conformation of erythro and threo forms of compounds related to ephedrine and isoetharine. *Acta Pharm. Suec.* **1977**, *14*, 30–36.
(43) Enders, D.; Eichenauer, H. Asymmetric syntheses via metalated chiral hydrazones. Enantioselective alkylation of cyclic ketones and aldehydes. *Chem. Ber.* **1979**, *112*, 2933–2960.
(44) Porath, B.; Rademacher, P.; Boese, R.; Bläser, D. Hydrogen bonding of 2-tetrazenes, 2. Synthesis and structural studies of hydroxyalkyl-substituted 2-tetrazenes. *Z. Naturforsch.* **2002**, *57*, 365–376.
(45) Clark, R. D.; Fox, P. C. Statistical variation in progressive scrambling. *J. Comput.-Aided Mol. Des.* **2004**, *18*, 563–576.
(46) Eriksson, L.; Jaworska, J.; Worth, A. P.; Cronin, M. T.; McDowell, R. M.; Gramatica, P. Methods for reliability and uncertainty assessment and for applicability evaluations of classification- and regression-based QSARs. *Environ. Health Perspect.* **2003**, *111*, 1361–1375.
(47) Henderson, A. R. The bootstrap: a technique for data-driven statistics. Using computer-intensive analyses to explore experimental data. *Clin. Chim. Acta* **2005**, *359*, 1–26.
(48) Holt, A.; Smith, D. J.; Cendron, L.; Zanotti, G.; Rigo, A.; Di Paolo, M. L. Multiple binding sites for substrates and modulators of semicarbazide-sensitive amine oxidases: kinetic consequences. *Mol. Pharmacol.* **2008**, *73*, 525−538.
(49) SYBYL 7.3, Tripos International: St. Louis, MI.
(50) Frisch, M. J.; Trucks, G. W.; Schlegel, H. B.; Scuseria, G. E.; Rob, M. A.; Cheeseman, J. R.; Montgomery, J. A.; Jr., Vreven, T.; Kudin, K. N.; Burant, J. C.; Millam, J. M.; Iyengar, S. S.; Tomasi, J.; Barone, V.; Mennucci, B.; Cossi, M.; Scalmani, G.; Rega, N.; Petersson, G. A.; Nakatsuji, H.; Hada, M.; Ehara, M.; Toyota, K.; Fukuda, R.; Hasegawa, J.; Ishida, M.; Nakajima, T.; Honda, Y.; Kitao, O.; Nakai, H.; Klene, M.; Li, X.; Knox, J. E.; Hratchian, H. P.; Cross, J. B.; Bakken, V.; Adamo, C.; Jaramillo, J.; Gomperts, R.; Stratmann, R. E.; Yazyev, O.; Austin, A. J.; Cammi, R.; Pomelli, C.; Ochterski, J. W.; Ayala, P. Y.; Morokuma, K.; Voth, G. A.; Salvador, P.; Dannenberg, J. J.; Zakrzewski, V. G.; Dapprich, S.; Daniels, A. D.; Strain, M. C.; Farkas, O.; Malick, D. K.; Rabuck, A. D.; Raghavachari, K.; Foresman, J. B.; Ortiz, J. V.; Cui, Q.; Baboul, A. G.; Clifford, S.; Cioslowski, J.; Stefanov, B. B.; Liu, G.; Liashenko, A.; Piskorz, P.; Komaromi, I.; Martin, R. L.; Fox, D. J.; Keith, T.; M. A. Al-Laham, Peng, C. Y.; Nanayakkara, A.; Challacombe, M.; Gill, P. M. W.; Johnson, B.; Chen, W.; Wong, M. W.; Gonzalez, C.; Pople, J. A. *Gaussian 03*; Gaussian, Inc.: Wallingford, CT, 2003.
(51) Bayly, C. I.; Cieplak, P.; Cornell, W. D.; Kollman, P. A. A well-behaved electrostatic potential based method using charge restraints for deriving atomic charges: The RESP model. *J. Phys. Chem.* **1993**, *97*, 10269.
(52) Wang, J.; Wang, W.; Kollman, P. A.; Case, D. A. Automatic atom type and bond type perception in molecular mechanical calculations. *J. Mol. Graph. Model.* **2006**, *25*, 247–260.
(53) Phillips, J. C.; Braun, R.; Wang, W.; Gumbart, J.; Tajkhorshid, E.; Villa, E.; Chipot, C.; Skeel, R. D.; Kale, L.; Schulten, K. Scalable molecular dynamics with NAMD. *J. Comput. Chem.* **2005**, *26*, 1781–1802.
(54) Duan, Y.; Wu, C.; Chowdhury, S.; Lee, M. C.; Xiong, G.; Zhang, W.; Yang, R.; Cieplak, P.; Luo, R.; Lee, T.; Caldwell, J.; Wang, J.; Kollman, P. A point-charge force field for molecular mechanics simulations of proteins based on condensed-phase quantum mechanical calculations. *J. Comput. Chem.* **2003**, *24*, 1999–2012.
(55) Wang, J.; Wolf, R. M.; Caldwell, J. W.; Kollman, P. A.; Case, D. A. Development and testing of a general amber force field. *J. Comput. Chem.* **2004**, *25*, 1157–1174.
(56) Feller, S. E.; Zhang, Y.; Pastor, R. W.; Brooks, B. R. Constant pressure molecular dynamics simulation: The Langevin piston method. *J. Chem. Phys.* **1995**, *103*, 4613.
(57) Schlick, T.; Skeel, R. D.; Brunger, A. T.; Kalé, L. V.; Board, J. A. J.; Hermans, J.; Schulten, K. Algorithmic challenges in computational molecular biophysics. *J. Comput. Phys.* **1999**, *151*, 9–48.
(58) Darden, T.; York, D.; Pedersen, L. Particle mesh Ewald: An W log(N) method for Ewald sums in large systems. *J. Chem. Phys.* **1993**, *98*, 10089–10092.
(59) Ryckaert, J.; Ciccotti, G.; Berendsen, H. J. Numerical integration of the Cartesian equations of motion of a system with constraints: molecular dynamics of *n*-alkanes. *J. Coput. Phys* **1977**, *23*, 327.
(60) Berman, H. M.; Westbrook, J.; Feng, Z.; Gilliland, G.; Bhat, T. N.; Weissig, H.; Shindyalov, I. N.; Bourne, P. E. The Protein Data Bank. *Nucleic Acids Res.* **2000**, *28*, 235–242.
(61) Lovell, S. C.; Word, J. M.; Richardson, J. S.; Richardson, D. C. The penultimate rotamer library. *Proteins* **2000**, *40*, 389–408.
(62) Lehtonen, J. V.; Still, D. J.; Rantanen, V. V.; Ekholm, J.; Björklund, D.; Iftikhar, Z.; Huhtala, M.; Repo, S.; Jussila, A.; Jaakkola, J.; Pentikäinen, O.; Nyrönen, T.; Salminen, T.; Gyllenberg, M.; Johnson, M. S. BODIL: a molecular modeling environment for structure-function analysis and drug design. *J. Comput.-Aided Mol. Des.* **2004**, *18*, 401–419.
(63) Halgren, T. A. Merck molecular force field. I. Basis, form, scope, parameterization, and performance of MMFF94. *Comput. Chem.* **1996**, *17*, 490–519.
(64) Jones, G.; Willett, P.; Glen, R. C. A genetic algorithm for flexible molecular overlay and pharmacophore elucidation. *J. Comput.-Aided Mol. Des.* **1995**, *9*, 532–549.
(65) Jones, G.; Willett, P.; Glen, R. C.; Leach, A. R.; Taylor, R. Development and validation of a genetic algorithm for flexible docking. *J. Mol. Biol.* **1997**, *267*, 727–748.
(66) Cramer, R. D., III; Bunce, J. D.; Patterson, D. E.; Frank, I. E. Crossvalidation, bootstrapping, and partial least squares compared with multiple regression in conventional QSAR studies. *Quant. Struct.-Activity Relationships* **1988**, *7*, 18–25.